DISCLAIMER

This report was prepared as an account of work sponsored by an agency of the United States Government. Neither the United States Government nor any agency thereof, nor any of their employees, makes any warranty, express or implied, or assumes any legal liability or responsibility for the accuracy, completeness, or usefulness of any information, apparatus, product, or process disclosed, or represents that its use would not infringe privately owned rights. Reference herein to any specific commercial product, process, or service by trade name, trademark, manufacturer, or otherwise does not necessarily constitute or imply its endorsement, recommendation, or favoring by the United States Government or any agency thereof. The views and opinions of authors expressed herein do not necessarily state or reflect those of the United States Government or any agency thereof. Reference herein to any social initiative (including but not limited to Diversity, Equity, and Inclusion (DEI); Community Benefits Plans (CBP); Justice 40; etc.) is made by the Author independent of any current requirement by the United States Government and does not constitute or imply endorsement, recommendation, or support by the United States Government or any agency thereof.

ANL/NSE-25/64
INL/RPT-25-88104

High-Temperature Gas-Cooled Reactors Multiphysics Simulation Demonstration and Code Validation

---

Nuclear Science and Engineering Division

About Argonne National Laboratory
Argonne is a U.S. Department of Energy laboratory managed by UChicago Argonne, LLC under contract DE-AC02-06CH11357. The Laboratory's main facility is outside Chicago, at 9700 South Cass Avenue, Lemont, Illinois 60439. For information about Argonne and its pioneering science and technology programs, see www.anl.gov.

DOCUMENT AVAILABILITY

Online Access: U.S. Department of Energy (DOE) reports produced after 1991 and a growing number of pre-1991 documents are available free at OSTI.GOV (http://www.osti.gov/), a service of the US Dept. of Energy's Office of Scientific and Technical Information.

Reports not in digital format may be purchased by the public from the National Technical Information Service (NTIS):

U.S. Department of Commerce
National Technical Information Service 5301
Shawnee Rd
Alexandria, VA 22312
www.ntis.gov
Phone: (800) 553-NTIS (6847) or (703) 605-6000
Fax: (703) 605-6900
Email: **orders@ntis.gov**

Reports not in digital format are available to DOE and DOE contractors from the Office of Scientific and Technical Information (OSTI):

U.S. Department of Energy
Office of Scientific and Technical Information
P.O. Box 62
Oak Ridge, TN 37831-0062
www.osti.gov
Phone: (865) 576-8401
Fax: (865) 576-5728
Email: **reports@osti.gov**

Disclaimer
This report was prepared as an account of work sponsored by an agency of the United States Government. Neither the United States Government nor any agency thereof, nor UChicago Argonne, LLC, nor any of their employees or officers, makes any warranty, express or implied, or assumes any legal liability or responsibility for the accuracy, completeness, or usefulness of any information, apparatus, product, or process disclosed, or represents that its use would not infringe privately owned rights. Reference herein to any specific commercial product, process, or service by trade name, trademark, manufacturer, or otherwise, does not necessarily constitute or imply its endorsement, recommendation, or favoring by the United States Government or any agency thereof. The views and opinions of document authors expressed herein do not necessarily state or reflect those of the United States Government or any agency thereof, Argonne National Laboratory, or UChicago Argonne, LLC.

ANL/NSE-25/64
INL/RPT-25-88104

High-Temperature Gas-Cooled Reactors Multiphysics Simulation Demonstration and Code Validation

---

prepared by
Zhiee Jhia Ooi, Thanh Hua, Hansol Park, Jun Fang, and Ling Zou
Nuclear Science and Engineering Division, Argonne National Laboratory

Joshua T. Hanophy, David Reger, Robert Kile, and Ryan H. Stewart
Idaho National Laboratory

September 2025

Page intentionally left blank

ABSTRACT

This study presents a comprehensive benchmarking and verification effort of several thermal-hydraulic and multiphysics capabilities for high-temperature gas-cooled reactor applications. The first part of this effort focuses on the running-in verification of Griffin's multiphysics capabilities, specifically for simulating the evolution of pebble-bed reactor cores from startup to equilibrium. Since Fiscal Year 2024, improvements and enhancements have been implemented in Griffin, including simplifying the process to specify streamlines and developing the online cross-section generation capability. In the absence of validation data, code-to-code comparisons are conducted with *kugelpy*, showing good agreement for integral quantities like k-eff predictions and predictions for maximum power density. However, accuracy issues are noted for more detailed quantities like the spatial distribution of fission rate densities which will require further work to address. The second part of this report presents an improved System Analysis Module (SAM) core channel model where the effects of cross flow are considered during the pressurized loss of forced cooling transient, resulting in an improved agreement of the predicted pebble temperature with respect to the predictions from the SAM 2D porous media model. Additionally, the wall channeling effect due to variable porosity at the near wall region of the core is also investigated. Furthermore, to demonstrate Griffin's online cross-section generation capability, a multiphysics simulation is performed by coupling Griffin to the SAM core channel model. In the third part of the report, as a part of the Organisation for Economic Co-operation and Development/Nuclear Energy Agency (OECD/NEA) thermal-hydraulic code validation benchmark activity for a high-temperature gas-cooled reactor, the High Temperature Test Facility (HTTF) is investigated first using the NekRS computational fluid dynamics (CFD) code to study the flow mixing phenomenon in the lower plenum of the facility. Then, code-to-code and code-to-data comparisons are performed for Test PG27, which is a pressurized conduction cooldown (PCC) test, using five different codes by six organizations from five countries. The different simulations show good agreements in terms of the general trend but there are differences in some results such as the peak temperatures of different regions and heat removal rate.

Page intentionally left blank

ACKNOWLEDGMENTS

Argonne National Laboratory's work was supported by U.S. DOE Office of Nuclear Energy's Nuclear Energy Advanced Modeling and Simulation (NEAMS) program, through U.S. Department of Energy contract DE-AC02-06CH11357. Idaho National Laboratory's work was supported by U.S. DOE Office of Nuclear Energy's Nuclear Energy Advanced Modeling and Simulation (NEAMS) program and Advanced Reactor Technologies Gas-Cooled Reactor (ART-GCR) program, through U.S. Department of Energy contract DE-AC07-05ID14517. This research made use of Idaho National Laboratory's High Performance Computing systems located at the Collaborative Computing Center and supported by the Office of Nuclear Energy of the U.S. Department of Energy and the Nuclear Science User Facilities under Contract No. DE-AC07-05ID14517.

Page intentionally left blank

CONTENTS

FIGURES

TABLES

ACRONYMS

ART-GCR	Advanced Reactor Technology - Gas-Cooled Reactor
CFD	computational fluid dynamics
CFL	Courant–Friedrichs–Lewy
COU	couplings
DCC	depressurized conduction cooldown
DEM	discrete element method
DLOFC	depressurized loss of forced cooling
DOE	U.S. Department of Energy
FY	Fiscal Year
GCPBR	gas-cooled pebble-bed reactor
GPBR200	200 MW General Pebble Bed Reactor
HTGR	high-temperature gas-cooled reactor
HTR-PM	High-Temperature Gas-cooled Reactor Pebble-bed Module
HTTF	High Temperature Test Facility
HTTR	High Temperature Engineering Test Reactor
INL	Idaho National Laboratory
LES	large eddy simulation
MHTGR	Modular High Temperature Gas-cooled Reactor
MOOSE	Multiphysics Object-Oriented Simulation Environment
NEAMS	Nuclear Energy Advanced Modeling and Simulation
OECD/NEA	Organisation for Economic Co-operation and Development/Nuclear Energy Agency
OSU	Oregon State University
PBR	pebble-bed reactor
PCC	pressurized conduction cooldown
PLOFC	pressurized loss of forced cooling
RCCS	reactor cavity-cooling system
RPV	reactor pressure vessel

SAM	System Analysis Module
SYS	System codes
TRISO	tristructural isotropic
VSOP	Very Superior Old Programs
VTB	Virtual Test Bed

Page intentionally left blank

High-Temperature Gas-Cooled Reactors Multiphysics Simulation Demonstration and Code Validation

M2MS-25AN0701021

1. INTRODUCTION

High-temperature gas-cooled reactors (HTGRs) are advanced nuclear systems that operate at high outlet temperatures and are typically helium cooled, graphite moderated, and fueled with tristructural isotropic (TRISO) particles. For their high thermal efficiency, inherent safety, and potential to provide high-temperature process heat, HTGRs have attracted worldwide interests. In the United States, X-energy is designing the Xe-100 reactor, which is a pebble-bed type of HTGR [1]. Valar Atomics and Nano Nuclear Energy are both pursuing a prismatic type of HTGRs. Other companies, such as HolosGen [2] and Boston Atomics [3], have also explored prismatic HTGR designs in a horizontal arrangement.

The unique design features of HTGRs, such as using coated fuel particles embedded in spherical pebbles or prismatic graphite blocks and passive decay heat removal systems, offer inherent safety and high thermal efficiency. At the same time, the combination of high-temperature operation, complex core geometries, and strongly coupled physical phenomena makes predictive modeling and simulating of HTGRs particularly challenging. An HTGR analysis inherently requires multiphysics simulations capabilities that couple reactor physics, fuel performance, thermal hydraulics, and chemical reactions (e.g., graphite oxidation). HTGR modeling also presents multiscale challenges to capture the behavior of submillimeter TRISO particles embedded in fuel pebbles and fuel rods in graphite matrix, pebble-to-pebble interactions in the core, full-core neutronics and flow fields, and core-scale heat transfer for decay heat removal.

For example, in pebble-bed HTGRs, simulating the run-in process, when fresh and burned pebbles and dummy graphite pebbles are continuously shuffled into the reactor core to gradually reach an equilibrium, requires simultaneously tracking stochastic pebble recirculation, evolving neutron flux distributions, fuel depletion, and thermal fluids. Capturing this dynamic equilibrium demands both discrete element methods (DEMs) for pebble motion and high-fidelity neutronic and thermal-fluid solvers. Similarly, air-ingress accident scenarios in prismatic or pebble-bed HTGRs highlight another multiphysics challenge. In the event of a breach in the pressure boundary of the primary system, the ingress of air can initiate graphite oxidation, altering both structural integrity and heat transfer properties of the core and potentially compromising the integrity of fuel, leading to the release of fission products. Accurate simulation of this scenario requires coupling multicomponent gas transport, molecular diffusion-dominant and buoyancy-driven flows, chemical kinetics of graphite oxidation, and the transport of fission products.

The Nuclear Energy Advanced Modeling and Simulation (NEAMS) program aims to accelerate the deployment of advanced nuclear energy technologies by developing predictive multiphysics modeling and simulation capabilities, including reactor physics, thermal hydraulics, fuel performance, and structural mechanics. Under the HTGR application driver work scope, we aim to support the modeling methodology development and code assessment, benchmark, validation, and demonstration of NEAMS tools for HTGR applications. Meanwhile, strong collaboration between NEAMS and U.S. Department of Energy (DOE) Advanced Reactor Technology - Gas-Cooled Reactor (ART-GCR) programs have been fostered to work on identified problems of interest to both parties, such as the ongoing High Temperature Test Facility (HTTF) benchmark and High Temperature Engineering Test Reactor (HTTR) benchmark as planned for future collaborations. The collaboration creates mutually beneficial feedback between the two DOE programs and a synergy combining the strengths of both programs, where the modeling and simulation capabilities developed under the NEAMS program are applied to solve real-world reactor-specific challenges as identified by the ART-GCR program.

2. PEBBLE-BED HTGR APPLICATIONS

2.1. Introduction To Streamline-Based PBR Modeling In Griffin

Schunert et al. introduced in detail the methodologies used by Griffin for modeling pebble-bed reactors (PBRs) in Reference [4]. That work focuses on equilibrium core calculations; the methodology used for running-in simulations is described by Hanophy et al. in Reference [5]. The modeling approach used by Griffin is based on the fact that the flow field describing pebble movement is very simple on the scale of tens to hundreds of pebbles. If one is not interesting in tracking the movement of individual pebbles, then it is accurate to say the flow field of pebbles in the core can be described by a few pathlines where the velocities are mostly constant in magnitude and direction along the entire pathline. With this in mind, Griffin requires a user to specify a few pathlines, which are used to describe the flow of pebbles in the entire core. The term streamline is used in Griffin instead of pathline, but the term streamline as used in Griffin is a pathline instead of the usual definition of streamlines in fluid flow. Streamline will subsequently be used in place of pathline in this report.

An example of an RZ-geometry mesh for modeling a gas-cooled pebble-bed reactor (GCPBR) is shown in Figure 1a. This mesh was generated based on the 200 MW General Pebble Bed Reactor (GPBR200) input available on the Virtual Test Bed (VTB) [6] at https://mooseframework.inl.gov/virtual_test_bed/htgr/gpbr200/index.html. The GPBR200 is a generalized model not based on any specific design that was created to be an open-source reference model. The mesh shown in Figure 1a is described in more detail in Reference [7]. As described in that work, the GPBR200 model includes multiphysics. In the model, Griffin is used to solve for power densities and these are passed to Pronghorn and BISON which compute temperatures. The mesh shown in Figure 1a is used for both the neutronics solve in Griffin and the thermal hydraulics solve in Pronghorn.

To model a PBR, streamline information must be provided by a user, as discussed at the beginning of this section. The streamlines used in the GPBR200 are shown in Figure 1b. These streamlines are specified as a piecewise continuous line with the user inputting the coordinates of each point in the line. In the simplest case where the core is modeled without any cones and the pebbles are assumed to move strictly downward, then the streamlines can be specified very simply with just one point at the inlet and one point at the outlet. The streamlines shown in Figure 1b were generated from a DEM simulation as described in Reference [8] by following the path of a pebble at several different distances from the center of the core. The streamlines shown in Figure 1b are relatively simple in the core region, but are more complicated in the lower cone. Specifying these lines on a point-by-point basis, while allowing flexibility, is very tedious and could be error prone for users. Even in the core region, the streamlines do move slightly and specifying the lines in this region requires more than a few points.

The pebble movement, burnup, and transmutation is modeled on the streamlines. But information about pebble nuclide compositions is needed on the neutronics mesh (Figure 1a) to compute cross sections. Griffin includes an algorithm to assign cells from the neutronics mesh to a streamline segment from which that cell gets nuclide compositions. Based on the streamlines shown in Figure 1a, the mesh cells are partitioned among the five streamlines as shown in Figure 1c.

2.1.1. Usability Enhancements for Specifying Streamlines

Based on the shape of the mesh shown in Figure 1a, the manner in which the cells have been partitioned, as shown in Figure 1c, is not surprising. In fact, the mesh itself was created based on the same pebble tracks used to specify the streamlines. The mesh shown in Figure 1b was generated in Multiphysics Object-Oriented Simulation Environment (MOOSE) using the MeshGenerator system. The MeshGenerator inputs to generate the mesh are somewhat complicated as there is no automated way to create lines following some particular trajectory, like that taken from DEM simulation output. However, work is being done to simplify

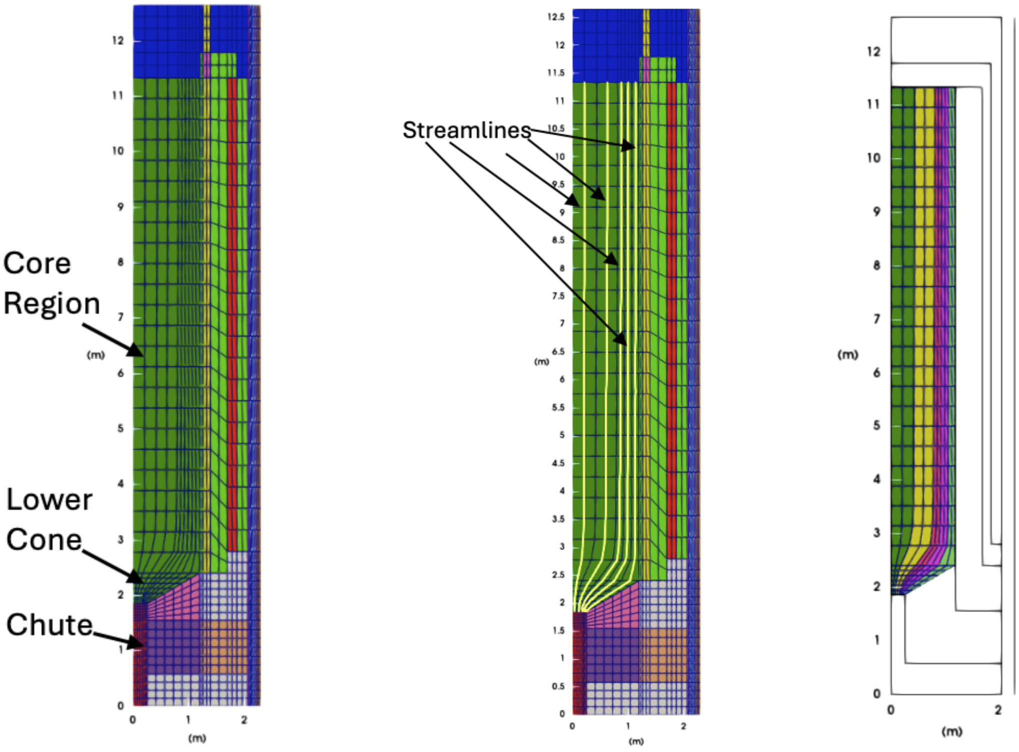

(a) (b) (c)

Figure 1. (a) A schematic of an RZ-geometry GPBR-200 Griffin model, (b) the GPBR-200 neutronics mesh showing pebble depletion streamlines, and (c) the core region of the GPBR-200 mesh shown with the mesh cells partitioned among the five streamlines.

the MeshGenerator inputs required to generate any GCPBR mesh, which would generally be similar to that shown in Figure 1a. Given a mesh that looks like this, there is a simpler way to specify the streamlines than having to specify the streamlines point by point. Specifying the streamlines point by point required inputting 150 points, each point being specified by inputting the point's three coordinates. This obviously required a huge amount of input which was time consuming to produce and could be prone to error.

A new mesh generator, named PebbleStreamlineIDGenerator, was created in Griffin this year to greatly simply specifying streamlines. The sample input used to add streamlines to a mesh similar to that shown in Figure 1a is shown in Figure 2. Instead of specifying many coordinates for a piecewise continuous line, all a user has to do is specify a few sidesets. Specifically, each streamline inlet sideset is specified and then a single sideset is specified that is a common outlet for all streamlines. Sidesets are simple to specify using MeshGenerators, with examples shown in Figure 3. In Figure 3a, SideSetsBetweenSubdomainsGenerator is used. This works when each streamline has already been coded into the mesh as a separate block, as might be done for multiple reasons. Another possible way to specify a streamline inlet boundary is shown in Figure 3b where a ParsedGenerateSideset MeshGenerator is used. This, for example, could be used when the entire core is a single block instead of the streamlines already having been separated. The MeshGenerator system is flexible and there are multiple ways to add sidesets. The new MeshGenerator PebbleStreamlineIDGenerator currently supports 2D meshes, but the overall approach is easily generalizable to 3D meshes, and this work is ongoing.

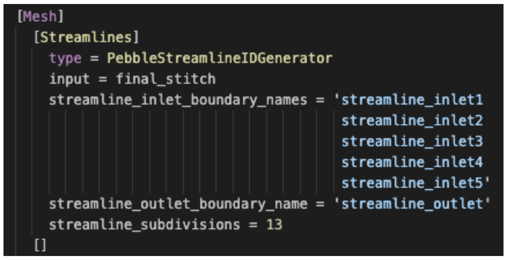

```
[Mesh]
  [Streamlines]
    type = PebbleStreamlineIDGenerator
    input = final_stitch
    streamline_inlet_boundary_names = 'streamline_inlet1
                                       streamline_inlet2
                                       streamline_inlet3
                                       streamline_inlet4
                                       streamline_inlet5'
    streamline_outlet_boundary_name = 'streamline_outlet'
    streamline_subdivisions = 13
  []
```

Figure 2. Input syntax shown for the new mesh generator that eases specifying streamlines.

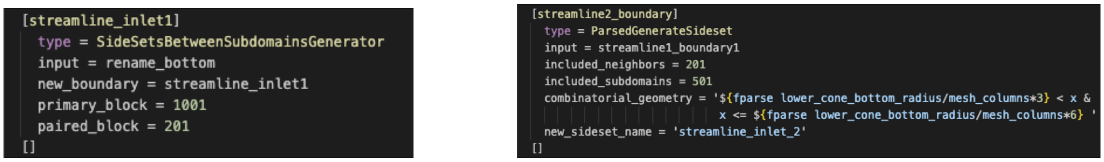

```
[streamline_inlet1]
  type = SideSetsBetweenSubdomainsGenerator
  input = rename_bottom
  new_boundary = streamline_inlet1
  primary_block = 1001
  paired_block = 201
[]
```

```
[streamline2_boundary]
  type = ParsedGenerateSideset
  input = streamline1_boundary1
  included_neighbors = 201
  included_subdomains = 501
  combinatorial_geometry = '${fparse lower_cone_bottom_radius/mesh_columns*3} < x &
                            x <= ${fparse lower_cone_bottom_radius/mesh_columns*6} '
  new_sideset_name = 'streamline_inlet_2'
[]
```

(a)

(b)

Figure 3. Two example ways that sidesets can be added to a mesh using (a) SideSetsBetweenSubdomainsGenerator and (b) ParsedGenerateSideset.

2.2. PBR Running-In Simulation Verification Progress

GCPBRs are initially made to go critical by first filling them with non-fueled graphite pebbles. Then, the pebble flow is started, and fueled pebbles are added to the top of the reactor to replace the graphite pebbles being removed from the bottom of the reactor. Eventually, enough fuel is added to the reactor that it goes critical. From this point onward, the reactor power is increased. It generally takes more than a year for the power to be increased from zero to the nominal operating level. Over several years, the reactor approaches an equilibrium configuration, the equilibrium core. This initial phase of PBR operation is referred to as running-in.

The capability for multiphysics running-in simulations with Griffin was demonstrated by Hanophy et al. in Reference [5]. There are few other published works that show multiphysics running-in simulation results. The Very Superior Old Programs (VSOP) code has been used for PBR analysis over many decades, and a multiphysics running-in simulation for the High-Temperature Gas-cooled Reactor Pebble-bed Module (HTR-PM) in China was published by Zhang et al. in Reference [9]. Both VSOP and Griffin implement deterministic methods for neutron transport calculations. A multiphysics running-in simulation that used a Monte Carlo based method for transport was published by Stewart et al. in Reference [10].

2.2.1. Revisiting an Equilibrium Fuel Injection Test Case

Multiple code-to-code scenarios relevant to running-in simulations were compared between Griffin and *kugelpy* in Reference [11]. That work will be referred to subsequently as the initial running-in verification study. This section contains updates to that work. Of particular interest among the code-to-code scenarios studied in the previous work was a simplified running-in scenario that started with a layer of non-fueled graphite pebbles up to near the critical height and above this a mix of 60% fueled pebbles and 40% non-fueled graphite pebbles. The initial fueled pebbles have a lower enrichment than the equilibrium fuel and are called starting fuel pebbles. The initial feed of pebbles replacing the non-fueled graphite pebbles leaving the bottom of the reactor was set to be 60% starting fuel pebbles and 40% non-fueled graphite pebbles until 80 days when the feed was switched to 100% equilibrium fuel. The core inventory of the different pebble types is shown throughout the simulation in Figure 4. For reference, the simplified Griffin model used in the initial running-in verification study is shown in Figure 5 with the specific dimensions being listed in Table 1 of Reference [11].

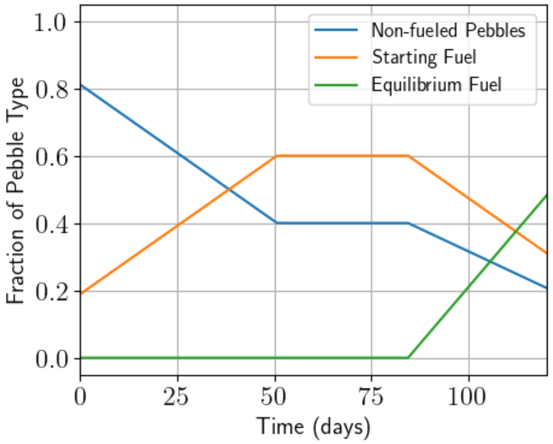

Figure 4. Fractions of the three pebble types in the PBR core throughout the benchmark simulation.

The scenario described above was investigated primarily for two features of the scenario. First, the simulation has sharp interfaces between regions where the pebble composition changes. Second, there are interesting simulation results related to when the equilibrium fuel is first introduced to the reactor. The sharp interface feature is discussed first.

kugelpy uses a Lagrangian-based method to model pebble flow as described in Reference [12] while Griffin uses a Eulerian-based approach, which can exhibit significant numerical diffusivity as described in Reference [5]. This numerical diffusivity means sharp interfaces may not be well modeled as they diffuse into diffuse interfaces. This issue was briefly discussed in the initial running-in verification study. The issue was somewhat obfuscated by the fact that the Griffin results presented in the previous work used a timestep set to 0.5× the Courant–Friedrichs–Lewy (CFL) number, which has typically been done for running-in simulations with Griffin. In this case, the relevant quantities to the CFL number are the PBR core mesh spacing and the flow velocity of the pebbles.

Typically, the pebble flow velocity will vary with time as the flow rate of pebbles is adjusted throughout the simulation. The pebble velocity can also vary across each streamline for the same mass flow rate if the porosity is different for different streamlines. However, a uniform porosity was used along with a constant pebble feed rate in the running-in simulations, and all mesh cells in the core region have the same dimension as shown in Figure 5. Because of this, the timestep can be set arbitrarily close to the CFL limit and the pebble flow will be arbitrarily close to the Lagrangian-based *kugelpy* result. The sharp interface resulting from taking a timestep 0.99× the CFL is shown in Figure 6. The fact that Griffin can be made to track a sharp interface well for the simple model used in these verification studies is used later in this updated analysis presented in this work to better investigate the importance of modeling the sharp interface.

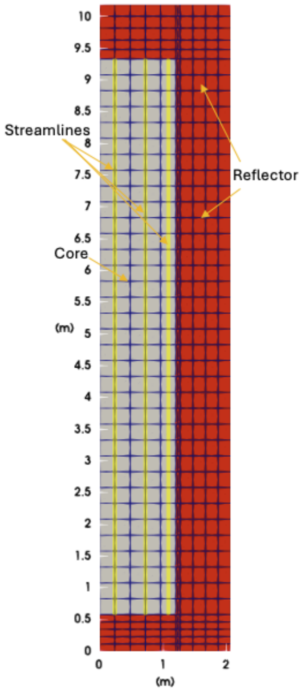

Figure 5. Simplified PBR model used for the code-to-code comparison studies presented in Reference [11] with the streamlines used marked in yellow.

In Reference [5], the first introduction of equilibrium fuel during the running-in simulation caused the maximum power density to increase significantly. A significant increase in the maximum power density was also seen in the *kugelpy* results published in Reference [12], but the metric report was an “average maximum” power density. Additionally, the running-in scenarios were different between References [5] and [12], so it was unclear if the increase in maximum power density predicted by Griffin was realistic. The results from the initial running-in verification study included a direct comparison of the maximum power density predictions between Griffin and *kugelpy*. As mentioned previously, the timesteps taken by Griffin and *kugelpy* did not agree as Griffin was using a time step based on 0.5× the CFL while *kugelpy* was taking a step equal to the CFL. The study was repeated with Griffin taking a step equal to 0.99× the CFL, and the predictions for k-eff and the maximum power density are compared between the two codes in Figure 7. The agreement in the predicted maximum power density is very similar between the codes, with a small difference right before the spike due to a slight difference in the exact timing for when the equilibrium fuel is introduced. Even with the timestep set to 0.99× the CFL number, the timestep used in Griffin does not exactly match the timestep

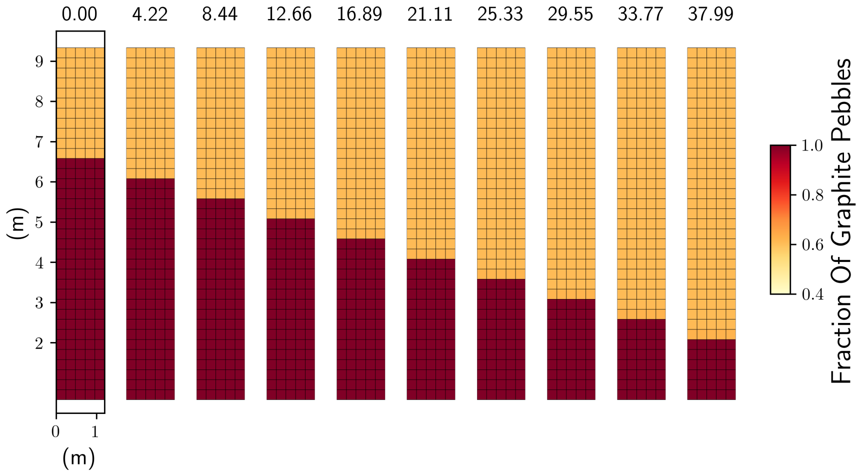

Figure 6. Fraction of non-fueled graphite pebbles in the core region with the time in days into the simulation shown above each plot.

used in *kugelpy*. Griffin and *kugelpy* are using the same core mesh spacing and have the same pebble flow velocity. But since *kugelpy* is a Lagrangian based code, it can take a time step given by 1.0 times the CFL number instead of some number less than one which must be taken by Griffin.

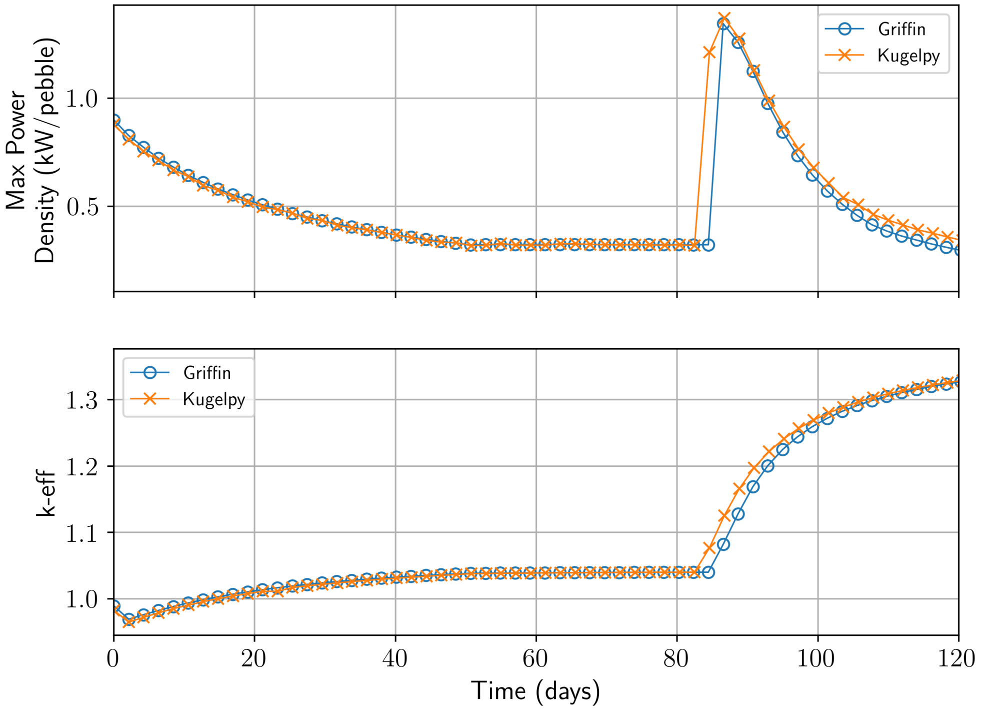

Figure 7. Maximum pebble power density and k-eff plotted throughout the benchmark simulation.

The results presented in Figure 7 used a pregenerated multigroup cross-section library. More details about the cross sections are included in Reference [11]. The multigroup library used was not generated from running-in but actually for an equilibrium core. While the pregenerated cross-section set has been used successfully for an equilibrium core analysis, its applicability to running-in is questionable since it was not developed for this purpose. Griffin now includes an online cross-section generation capability, which removes the need to pregenerate a library for a specific configuration. This is discussed further in Section 2.2.2. But given that the pregenerated multigroup library used was not designed for running-in simulations, the good agreement shown in Figure 7 might indicate that the maximum power density result is not very sensitive to the accuracy of the multigroup cross sections. This validates some of the Griffin running-in results presented in Reference [5], which also used a pregenerated multigroup library that had been developed for equilibrium for modeling.

Integral results, such as the maximum power density or k-eff, might match well between two models while more detailed results, such as the fission power distribution, could be significantly different. In general, it is expected that kugelphy and Griffin simulation results will differ when using a pregenerated multigroup library that was developed for an equilibrium core. In the initial running-in study, fission rate distributions were only compared at one particular time and the comparison was qualitative. A quantitative comparison that also includes more data is presented here. First, a more detailed comparison for the k-eff predictions is shown in Figure 8 where the differences are easier to see than with the scale in Figure 7.

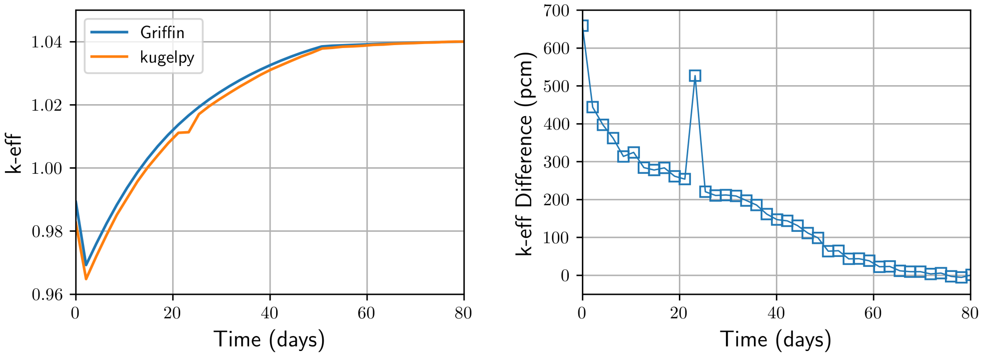

Figure 8. k-eff predictions for the first 80 days and the prediction difference between Griffin and *kugelpy*.

The maximum k-eff difference seen in Figure 8 is at the first timestep, with Griffin predicting a higher k-eff by approximately 700 pcm. The difference generally decreases through the initial part of the simulation, becoming nearly zero by 80 days. This may indicate that the sharp interface between the fueled and non-fueled regions is in fact leading to significant differences between *kugelpy* and Griffin since this interface moves down the core (as can be seen in Figure 6) in a similar trend to the decrease in k-eff difference. Figure 9 shows the relative difference in predicted fission rate between Griffin and *kugelpy*. This figure shows that the difference in predictions is dominated by the region near the reflector. This is not surprising necessarily because the pregenerated multigroup cross-section set had no leakage correction treatment. But an important feature of this plot is that the difference in fission rate predictions at the interface between the fueled and non-fueled region is small. It appears the primary reason the k-eff difference seen in Figure 8 decreases in time is that the volume of peripheral elements relative to the total core volume decreases as the core fills with more fuel. The takeaway is that potential modeling inaccuracies from not tracking a sharp interface well are much smaller than other issues. The large difference in fission rate predictions near the reflector could be remedied by additional work when pregenerating the multigroup library. However, Griffin now includes a capability for online cross-section generation where Griffin can generate its own cross sections. This eliminates the need for an analyst to have knowledge of a different code and use that separate code to generate cross sections for use in Griffin. This is discussed further in Section 2.2.2.

Given the relatively large difference in the predicted fission rates near the reflector shown in Figure 9, further investigating the good agreement in the maximum power density shown in Figure 7 is warranted.

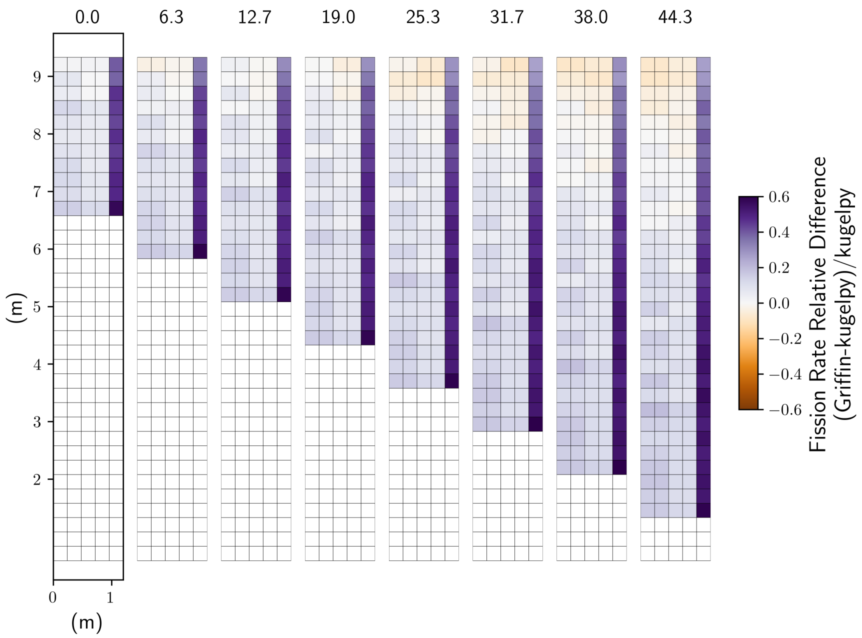

Figure 9. Relative difference in the fission rate predictions between Griffin and *kugelpy* during the first 45 days of the simulation. The labels on top of the plots are the simulation time in days.

The fission rate predictions for *kugelpy* and Griffin are shown in Figure 10. Comparing these two figures indicates how a simple metric like the maximum power density can be in good agreement between the two codes. The maximum power occurs right when the equilibrium fuel is introduced (the second plot in each subfigure) and specifically occurs near the center of the core. But it is apparent in Figure 10 that there are significant differences in the predicted fission rate distribution despite the maximum power density being very similar. It is not necessarily realistic that the power density would peak at the very top of the core. In reality, control rods would be inserted to some depth and the equilibrium fuel would need to move downward beyond the control rod depth before potentially experiencing a high power density. Control rods were not included in the initial running-in verification studies. An initial investigation of running-in scenarios that include control rods is included in Section 2.2.3.

2.2.2. Initial Evaluation of Online Cross-Section Generation

The online cross-section generation capability for Griffin was first introduced by Park et al. in Reference [13] for GCPBRs. Until this fiscal year, the assessment of the online cross-section capability had focused on the equilibrium core and various test fresh core configurations. The capability was first tested for a running-in simulation this fiscal year. Some initial work with the Griffin development team was required to get the capability functioning for the running-in simulations presented in the previous section.

With the code updates made this fiscal year, the online cross-section generation can be used for a running-in scenario. Accuracy issues are still being investigated. Figure 11 shows the simulation capability at the end of this fiscal year. The full transient can be simulated, but there are several obvious issues to be addressed in the future. There is a persistent positive bias in the k-eff prediction before 80 days of approximately 2,000 pcm. Additionally, the spike in the maximum power density when the equilibrium fuel is introduced is not being captured properly.

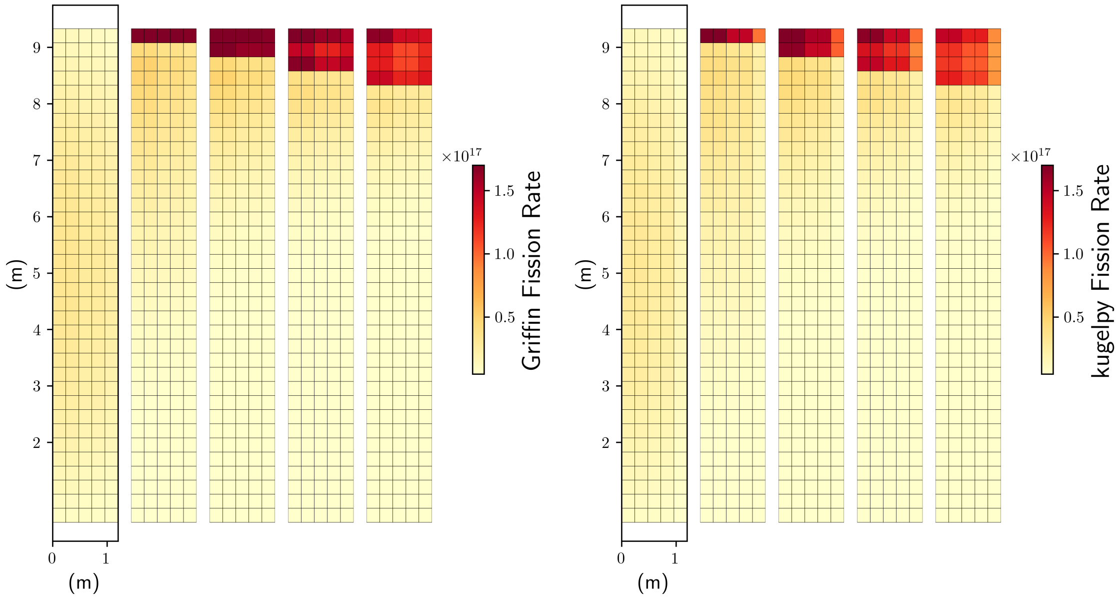

(a)

(b)

Figure 10. Fission rate predictions for (a) Griffin and (b) *kugelpy* when the equilibrium fuel is introduced and three timesteps beyond that point.

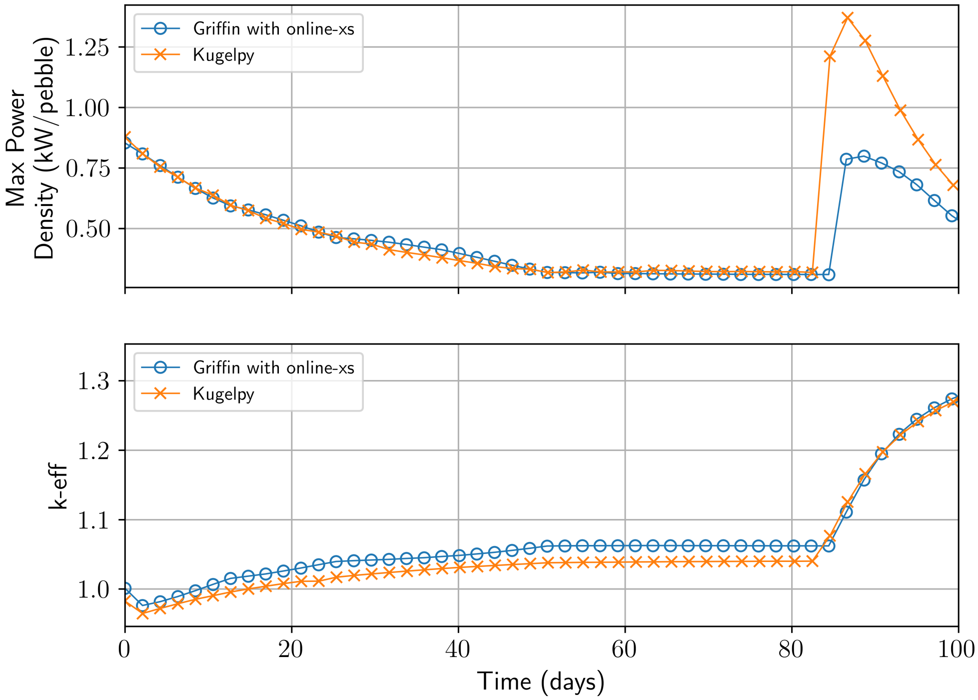

Figure 11. Maximum pebble power density and k-eff plotted throughout the benchmark simulation with Griffin using online cross-section capabilities.

2.2.3. Control Rod Studies

As discussed in Section 2.2.1, the situation shown in Figure 10 for the simple running-in benchmark case is not realistic because there would normally be control rods inserted in the top of the core. The equilibrium fuel would have to move downward some distance beyond the control rod front before it would experience a spike in power density. Models were developed this fiscal year both with *kugelpy* and Griffin that included control rods. The models have the same geometry as that shown in Figure 5.

The same scenario described in Section 2.2.1 (described in more detail in Reference [11]) was used again in an initial control rod study. Control rods were inserted 2.33 m into the core, and the critical height of the interface between the fueled and non-fueled region was moved downward so that the simulation starts near a k-eff equal to one. The *kugelpy* simulation results for the newly developed simulation are compared to the simulation without control rods in Figure 12. This figure shows that the same general trends are present in the simulation when control rods are added as in the simulation without control rods. The accuracy issues noted in Section 2.2.2 will be addressed in the future, and then the models developed with control rods will be useful for further verification of the Griffin running-in simulation capabilities.

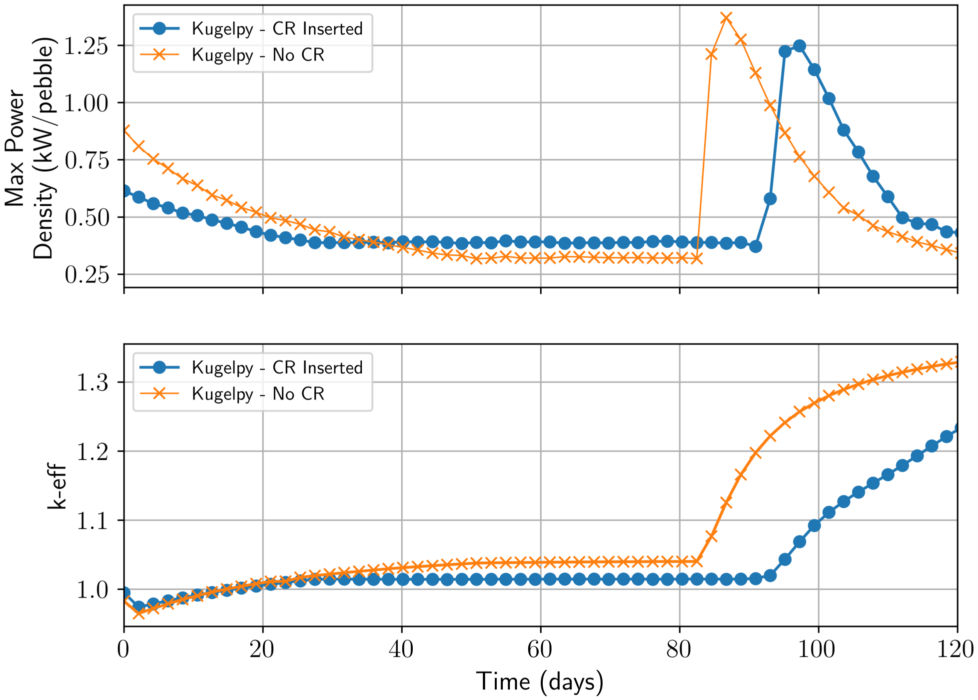

Figure 12. Maximum pebble power density and k-eff for the running-in benchmark simulation compared for the case with and without control rods.

2.3. System-Level PB-HTGR Simulations

2.3.1. Motivation

Compared with the conventional light-water reactors, the PBRs have complex core geometries that result in more complex thermal-fluid behaviors in the reactor core during both steady-state normal operating conditions and transient scenarios. Furthermore, the reactor reliance on a reactor cavity-cooling system (RCCS) for decay heat removal during certain transients introduces further challenges that need to be resolved in the modeling of these reactors. In the conventional light-water reactors, heat is removed primarily through convective heat transfer between the fuel rods and the coolant during both steady-state operating conditions and transient scenarios. The only differences are the source of the coolant (e.g., driven by coolant pumps compared with injection by emergency core cooling systems) and the switch from single-phase convective heat transfer to two-phase boiling heat transfer. On the other hand, for PBRs and other HTGR designs in general, the heat removal mechanisms during steady-state operating conditions and transient scenarios could be substantially different.

Under steady-state operating conditions, similar to light-water reactors, heat is removed mainly by forced convection between fuel pebbles and the coolant, with the coolant being some type of gas rather than water. However, during loss-of-forced-flow transient scenarios, unlike light-water reactors, decay heat is primarily removed from the core via radial heat conduction from the fuel pebbles to the side reflectors and finally to the RCCS. In the former, heat transfer is a localized phenomenon with a relatively small length scale on the order of several centimeters. Conversely, during loss-of-forced-flow transient scenarios, the core-wise radial conduction from the pebble bed to the RCCS adds another heat transfer length scale that corresponds to the reactor core diameter on the order of several meters. Furthermore, natural convection can establish in the core during the loss-of-forced-flow transients, which can further impact the temperature redistribution inside the reactor core and thus the removal of decay heat. The combination of different heat removal mechanisms poses a unique set of challenges to modeling PBRs.

Various modeling approaches for PBRs have been demonstrated by researchers, ranging from the unit-cell approach by van Antwerpen et al. [14] to study local heat transfer phenomena to full-scale large eddy simulation (LES) by Merzari et al. [15] using Cardinal, which is a lower length scale simulator that comprises three physics: neutronics, thermal fluids, and fuel performance. Additionally, the simulations of PBRs with Pronghorn using the porous medium approach have been demonstrated by other researchers [16–18].

In previous Fiscal Years (FYs), a model of the GPBR200 was developed with System Analysis Module (SAM) using the so-called core channel approach [19, 20]. In this approach, the core channel component in SAM is used to model the pebble bed of the GPBR200. The core channel is a SAM built-in component that consists of a 1D fluid component coupled to a 2D heat structure. Compared to the higher fidelity methods mentioned above, the core channel approach is faster and requires significantly fewer computational resources due to its lower resolutions and the use of correlations to solve for quantities such as pressure drop and heat transfer coefficients. As a result, despite the lower fidelity, the core channel approach is ideal for simulating long transients, such as the loss-of-forced-flow accidents.

In FY24, the core channel model was compared with a 2D SAM porous media model [21]. The core channel model showed good agreement with the higher fidelity porous media model for steady-state normal operating condition and depressurized loss of forced cooling (DLOFC) accident. However, the core channel model overpredicted the maximum and average pebble temperatures for the pressurized loss of forced cooling (PLOFC) accident. It was postulated that the overprediction of pebble temperature by the core channel model was due to the lack of the ability to model cross flow between the individual core channels during the PLOFC where in-core natural circulation played an important role of distributing the decay heat in the core.

The work in FY25 is a continuation from previous year's modeling efforts. Further investigation into interchannel cross flows was conducted. Furthermore, the core channel and 2D porous media models were updated to reflect the higher porosity at the near wall region of the core. In the coming sections, the core channel and porous media models are briefly described, followed by discussions on the progress accomplished in FY25.

Additionally, efforts have been made to demonstrate the Griffin-SAM coupled system using Griffin's online cross-section capability, which has been verified for a pebble-bed problem [13]. Because pregenerating cross sections for a PBR is not a straightforward task, this capability is valuable to users as it eliminates the burden of manual cross-section preparation. As an initial step, the online cross-section generation module was demonstrated only for a steady-state problem in FY25, and the results are discussed in this report.

2.3.2. SAM Core Channel Model

The GPBR200 reactor is chosen as the reference design in this work, focusing only on the core. Auxiliary components that make up the coolant system of the reactor are not included here to reduce the complexity of the model so that the thermal hydraulics behavior of the core could be properly studied. The design information of the reactor used here is obtained from the work by Stewart et al. based on publicly available figures and models [18]. The reactor has an installed thermal capacity of 200 MW, cooled by pressurized helium gas with the primary coolant pressure of 6 MPa, inlet and outlet core temperatures of 533 K and 1023 K, respectively, and a nominal helium mass flow rate of 78.6 kg/s during steady-state normal operating conditions. The pebble-bed core has a packing factor of 0.61, and roughly 223,000 pebbles are loaded. The schematic of the GPBR200 core is shown in Figure 13, and the dimensions of the core are tabulated in Table 1.

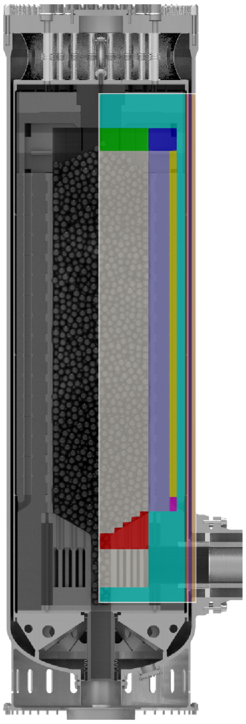

Figure 13. Schematic of the core of the GPBR200 [18].

Based on the schematic shown in Figure 13 and the dimensions tabulated in Table 1, a SAM model for the GPBR200 core is built. The schematic of the SAM model is shown in Figure 14 with the assumption that the core is axially symmetric. In the SAM model, solid structures, such as the reflectors, core barrel, reactor pressure vessel (RPV), and RCCS panels, are modeled with the `PBCoupledHeatStructure` components. Meanwhile, coolant channels, such as the upcomer and flow channels, in the bottom reflector are modeled as 1D flow with the `PBOneDFluidComponent`.

The pebble bed is modeled with multiple `PBCoreChannel` components where each of which effectively represents an annular region of a pebble bed. Note that the `PBCoreChannel` is essentially a 1D fluid component with built-in heat structures that can simulate solid-to-fluid thermal-fluid behaviors. This allows the specification of hydraulic parameters, such as flow area, hydraulic diameter, and surface roughness, as well as solid parameters, such as the geometry and material properties of the heat structure. Additionally, heat transfer parameters, such as the heat transfer area density, can be provided to the component. Solid, fluid, and heat transfer behaviors are then calculated internally by the `PBCoreChannel` component according to the

Table 1. Dimensions of the GPBR200 core [18].

Features	Dimensions [m]
Core Radius	1.20
Reflector Width Between Core and Riser	0.52
Riser Width	0.18
Outer Reflector Width	0.21
Gap Between Reflector and Barrel	0.04
Barrel Thickness	0.04
Gap Between Barrel and RPV	0.08
RPV Thickness	0.09
Bottom Reflector Height	0.54
Core Height	8.91
Core Inlet Height	0.36
Riser Height	8.57
Top Gap Height	0.55
Top Reflector Height	0.85

provided information. The `PBCoreChannel` component is set to have spherical heat structures where the heat transfer geometry is set as a pebble bed. The use of multiple `PBCoreChannels` in the radial direction allows the model to capture the radial heat conduction within the pebble bed and from the pebble-bed core to the reflectors, which is particularly important for loss-of-forced-flow transient scenarios where radial conduction plays a significant role in decay heat removal.

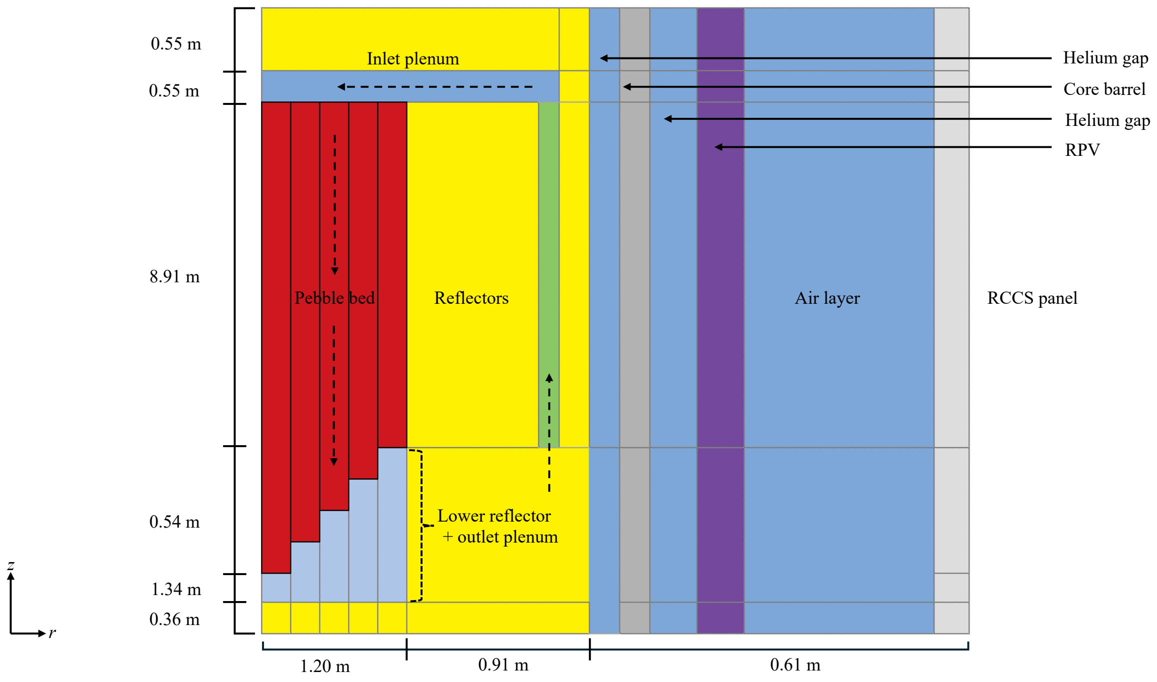

Figure 14. Schematic of the GPBR200 core for the SAM models (not to scale).

The core channels used to model the pebble-bed core are essentially independent of each other. To allow for heat conduction between the core channels, the heat structures of the core channels need to first be thermally coupled to each other. In SAM, the thermal coupling of heat structures can be accomplished through the `SurfaceCoupling` component where the heat transfer rate is determined by a user-defined heat transfer coefficient, called h_{gap} in SAM. Based on the units of heat transfer coefficient, h_{gap} is determined as function of the core-wide effective thermal conductivity, k_{eff}, and a length scale, L.

The k_{eff} is determined using the ZBS correlation, which calculates the effective thermal conductivity of the pebble-bed core considering the pebble-pebble conduction, pebble-coolant convection and conduction, and pebble-pebble radiation [22, 23]:

$$\frac{k_{eff}}{k_f} = \left(1 - \sqrt{1-\varepsilon}\right)\varepsilon\left[\left(\varepsilon - 1 + \frac{1}{\kappa_G}\right)^{-1} + \kappa_r\right] + \sqrt{1-\varepsilon}\left[\varphi\kappa + (1-\varphi)\,\kappa_c\right], \tag{1}$$

where φ is the surface fraction parameter for heat transfer through contact areas and ε is the porosity of the pebble-bed core. The nondimensional effective thermal conductivity related to fluid phase conduction, κ_G, is simplified to be 1. For the nondimensional effective thermal conductivity related to thermal radiation, κ_r, and the contribution from the heat transfer due to solid conduction, fluid conduction, and thermal radiation, κ_c, more detailed descriptions are available from other researchers [22, 23].

Given h_{gap} dictates the heat transfer rate between adjacent core channels and hence the rate of radial heat conduction between adjacent core channels, the modeling of h_{gap} is further examined. In this work, h_{gap} is calculated as:

$$h_{gap} = \frac{k_{eff}}{\Delta L} \cdot \frac{A_{channel}}{A_{pebbles}}, \tag{2}$$

where ΔL is defined as the distance between the centers of adjacent core channels or heat structures, $A_{channel}$ is the surface area of core channels, and $A_{pebbles}$ is the total surface area of pebbles in each core channels. The area ratio is used to account for the difference between the surface area of a core channel and the total surface area of pebbles in that channel. This approach to couple adjacent core channels has been validated using experimental data from the High Temperature Test Unit in FY23 [20].

A simplified natural-circulation-driven and water-cooled RCCS loop is added to the model. It is loosely based on the RCCS design used in the HTR-PM reactors [24]. A schematic of the closed-loop RCCS is shown in Figure 15. The loop consists of an RCCS panel of equal height to the core and is thermally coupled to a riser channel. Downstream of the riser is the unheated chimney section and the inventory tank. A heat exchanger is added to the tank as the ultimate heat sink. The secondary side of the heat exchanger is not modeled. Instead, the inlet and outlet boundary conditions on the secondary side are modeled using a time-dependent junction and a time-dependent volume, respectively. The cooled water flows from the inventory tank back to the riser through the downcomer. Heat transfer from the external wall of the RPV to the internal wall of the RCCS panel occurs through thermal radiation. Natural convection happening in the enclosure between the RPV and the RCCS panel is not currently modeled. The loop is assumed to be at atmospheric pressure.

2.3.3. SAM Porous Media Models

The SAM porous media model consists of three individual models, namely the core, the primary loop, and the RCCS loop. The core is modeled using SAM's multidimensional flow model in a 2D RZ geometry while the primary loop and RCCS are modeled with SAM's 0D and 1D components. The individual models are coupled to each other through the MOOSE MultiApp system [25].

The mesh of the 2D RZ core of the porous media model is shown in Figure 16. The pebble bed and the bottom reflectors are modeled as porous media while the side reflectors, core barrel, helium gaps, and RPV are modeled as solid. Note that the inlet and outlet plena are not modeled in the 2D porous media model but are instead modeled as 0D volume branches using the SAM component system in the primary loop model.

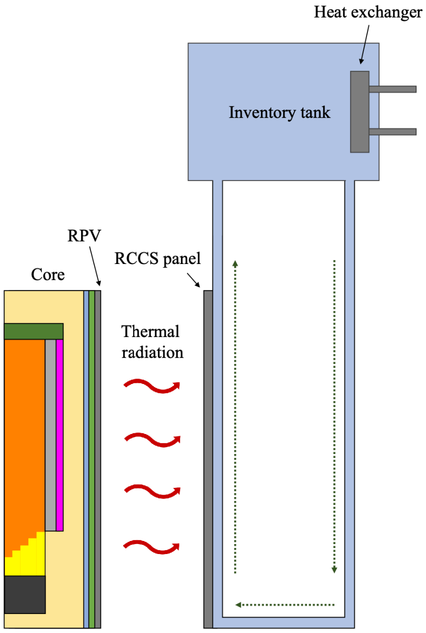

Figure 15. Schematic of the water-cooled closed-loop RCCS.

On the other hand, the riser is modeled using an approach that utilizes both the 2D meshes and the 1D component system. In the 2D model, even though the riser is meshed, it is treated as a solid component (rather than porous media) whose thermal physical properties are reduced by a factor of $1 - porosity$. This means that, in the 2D mesh, there is no fluid flow in the riser. Instead, the fluid flow in these two channels are modeled as 1D flow using `PBOneDFluidComponent` in the primary loop model. Conjugate heat transfer between these channels with the surrounding 2D solid structures is also modeled. This combined approach avoids the need to mesh the two channels in the 2D model while still capturing the radial heat conduction from the core to the surrounding reflectors.

The primary loop model essentially consists of three individual models. These are the cold leg, consisting of the riser, cold plenum, and inlet and outlet boundary conditions; the hot leg, consisting of the hot plenum, outlet channel, and inlet and outlet boundary conditions; and the surrogate channel with inlet and outlet boundary conditions. The surrogate channel is needed for the domain overlapping approach. The so-called domain overlapping approach is used to couple the 2D core model with the 0D/1D primary loop model [21]. Finally, the RCCS loop is the same as that used in the core channel model, as described in Section 2.3.2. The coupling between the core, primary loop, and RCCS models is accomplished through the MOOSE MultiApp system [25], with the porous media model acting as the `MainApp` and the other two models as the `SubApps`.

2.3.4. Cross Flow Development in SAM Core Channel Model

In FY24, the results from the SAM core channel model was compared against the results of the higher fidelity SAM 2D porous media model [21]. The core channel model performed relatively well during steady state and the DLOFC transient. However, the model showed a large overprediction of pebble temperatures during the PLOFC transient. An illustration of the flow paths of the 0D/1D core channel model during PLOFC is shown alongside the flow pattern predicted by the SAM 2D porous media model in Figure 17. In the 2D model, with the formation of natural circulation, helium flows upward in the hotter inner core region and downward in the cooler outer region. Based on the streamlines of the flow, significant cross flows occur near the outer region of the core where the downward flow consistently changes direction and flows upward before

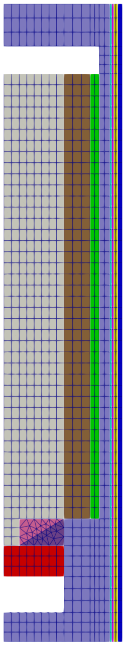

Figure 16. Mesh of the 2D RZ core of the SAM porous media model.

reaching the bottom of the core. This in turn increases core-wide mixing of hot and cold helium, improves the redistribution of heat from the hotter to cooler regions of the core, and eventually enhances the loss of decay heat from the core to the reflectors. Conversely, in the core channel model, even though natural circulation is formed, direction changes of the flow only occur at the top and bottom plenum. Unlike in the porous media model, the helium in the outermost channel has to flow downward for the whole length of the core. As a result, there is no mixing between helium flows in individual channels in the core, which results in poorer removal of decay heat to the surrounding reflectors.

Figure 18 compares the velocity profiles predicted by the SAM core channel and porous media models during PLOFC from FY24 [21]. The velocities are obtained at the top and bottom of the pebble bed at five radial locations denoted as CH-1–CH-5. In the porous media model, the velocities are the mean values obtained from r_{in} = [0, 0.36, 0.57, 0.78, 0.99] to r_{out} = [0.36, 0.57, 0.78, 0.99, 1.2]. Note that positive values represent downward flows and negative values represent upward flows. In the core channel model, CH-1–CH-4 show upward flows while a downward flow only happens in CH-5. Even though the core channel model is able to show natural circulation in the core, due to its inability to model cross flow, the direction change can only happen in the top and bottom plena. This means that flow in each channel has to travel the entire length of the core channel before the flow direction changes. This is evident in Figure 18(a) where the flow directions at the top and bottom of the core are always the same. On the other hand, the porous media model shows that the flow directions at the bottom and top of a channel are not always the same due to cross flows. For example, in the first 20 hours of the transient, the top and bottom velocities in CH-1–CH-3 have the same upward flow directions. However, this changes from t = 20 hours onward as the bottom velocities become downward while the top velocities remain upward due complex flow features, such as the formation of vortices. The existence of cross flows in the porous media model also enhances mixing in the core that improves heat transfer from the hotter inner core to the colder outer core.

An attempt is made to model cross flow in the SAM core channel model. In this approach, the cross flow between two channels is driven by the pressure difference between the adjacent nodes in the two channel, which itself results from the temperature difference between the nodes. A schematic of the cross flow model

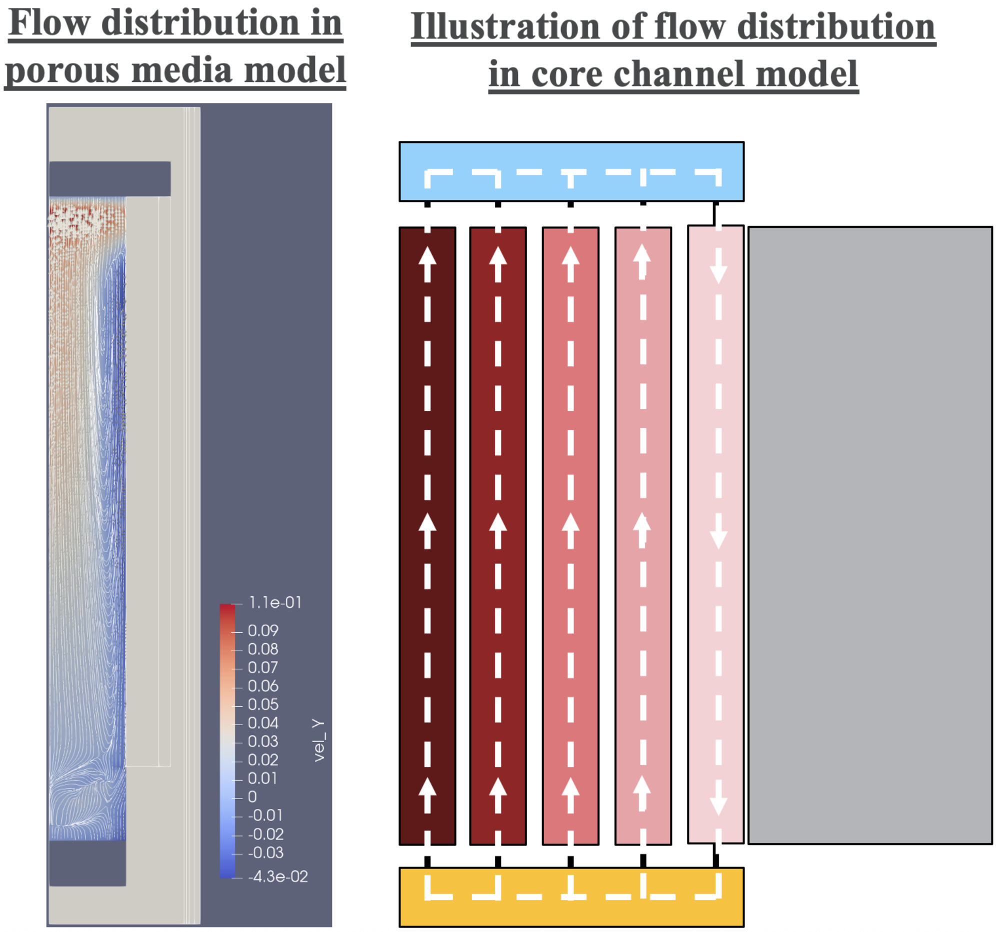

Flow distribution in porous media model

Illustration of flow distribution in core channel model

Figure 17. Comparison of natural circulation flow patterns in the 2D SAM porous media model and the 0D/1D SAM core channel model.

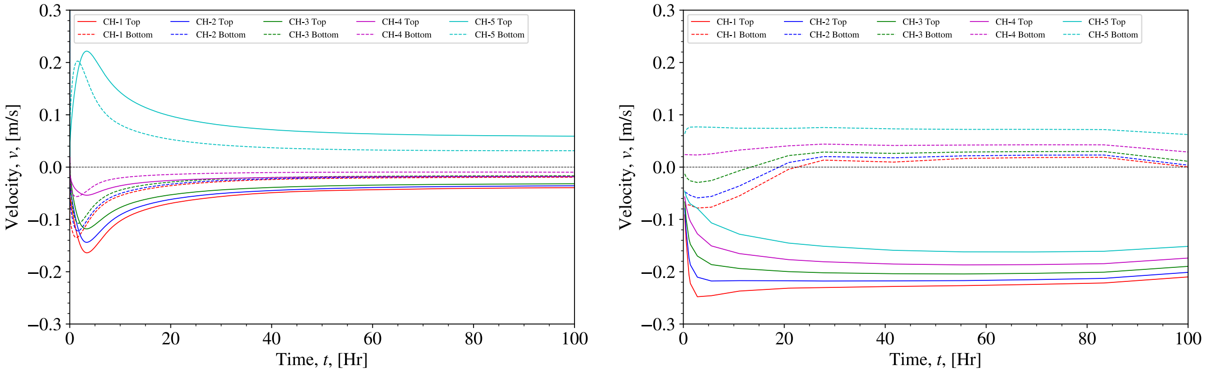

(a)

(b)

Figure 18. Comparison of the velocity profiles between the (a) core channel and (b) porous media models during a PLOFC. Positive values represent downward flows and negative values represent upward flows.

is shown in Figure 19 with two 1D core channels. Assuming that the pressure at node-1 (P_1) is greater than the pressure at node-2 (P_2) the cross flow is driven from node-1 to node-2. In this case, mass is leaving node-1 and entering node-2 where the transfer of mass between the two nodes can be modeled as volumetric sink and source terms.

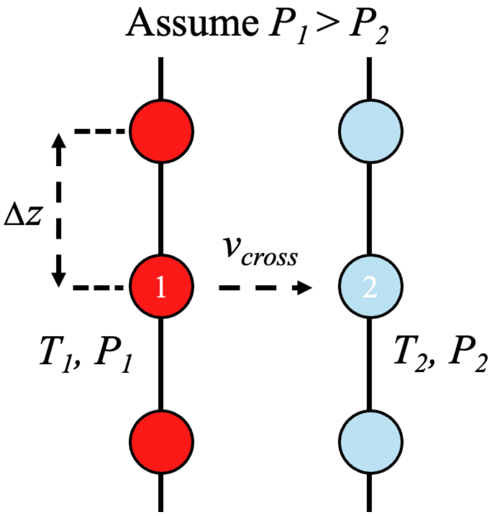

Figure 19. Schematic of the cross flow model in the SAM 1D core channel model.

In the SAM 1D fluid model, the mass conservation equation is given as,

$$\frac{\partial \rho}{\partial t} + \frac{\partial (\rho u)}{\partial z} = 0, \tag{3}$$

where u is the velocity in the axial direction. With the cross flow model, mass source and sink terms are added to the mass conservation equations as,

$$\frac{\partial \rho_1}{\partial t} + \frac{\partial (\rho_1 u_1)}{\partial z} = -\rho_{up} v_{cross} \frac{2\pi r_{int}}{A_1}, \tag{4}$$

$$\frac{\partial \rho_2}{\partial t} + \frac{\partial (\rho_2 u_2)}{\partial z} = \rho_{up} v_{cross} \frac{2\pi r_{int}}{A_2}, \tag{5}$$

where the subscripts 1 and 2 indicate the node number, v_{cross} is the cross flow velocity, A is the channel flow area, r_{int} is the interface radius between the two channels, and ρ_{up} is the upstream density, which in this case is the density of node-1.

The 1D energy conservation equation in SAM is given as,

$$\frac{\partial (\rho H)}{\partial t} + \frac{\partial (\rho u H)}{\partial z} = q''', \tag{6}$$

where H is enthalpy and q''' is the volumetric heat source. Similarly, with the cross flow model, a volumetric enthalpy sink or source term is added to the conservation equation as,

$$\frac{\partial (\rho_1 H_1)}{\partial t} + \frac{\partial (\rho_1 u_1 H_1)}{\partial z} = -H_{up} \rho_{up} v_{cross} \frac{2\pi r_{int}}{A_1}, \tag{7}$$

$$\frac{\partial (\rho_2 H_2)}{\partial t} + \frac{\partial (\rho_2 u_2 H_2)}{\partial z} = H_{up} \rho_{up} v_{cross} \frac{2\pi r_{int}}{A_2}, \tag{8}$$

where H_{up} is the upstream enthalpy, which in this case is the enthalpy of node-1.

The cross flow velocity, v_{cross}, is calculated using the Darcy–Weisbach equation based on the pressure difference between the two nodes,

$$\Delta P = f \frac{\rho_{up}}{2} \frac{v_{cross}^2}{Dh} L, \tag{9}$$

where f is the user-provided friction factor, L is the distance between the two nodes, and D_h is the hydraulic diameter.

A simple problem consisting of two parallel channels is set up to test the cross flow model. As shown in Figure 20, the two parallel channels have the same inlet velocity of 1.0 m/s and outlet pressures of 1.0×10^5 Pa and 1.05×10^5 Pa, respectively. Due to pressure difference, some flow is expected to be driven from Channel-2 to Channel-1.

The pressure and velocity profiles of the two channels with and without the cross models are shown in Figures 21 and 22, respectively. Without the cross flow model, the pressure in both channels drops linearly from the inlet to the outlet. Conversely, with the cross flow model, the pressure profiles in both channels appear to be slightly nonlinear. Furthermore, when the cross flow model is available, the pressure at the inlet of CH-2 is lower whereas the pressure at the inlet of CH-1 is higher due to the exchange of mass between the two channels. In Figure 22(a), both channels have the same velocity profile of 1 m/s from throughout the length of the channel without the cross flow model. On the other hand, with the cross flow model, the flow in CH-1 shows acceleration in the flow as it gains mass, whereas the flow in CH-2 shows deceleration as it loses mass. However, spatial oscillations are observed in the velocity profiles of both channels.

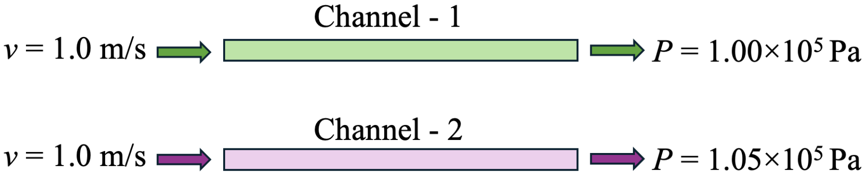

Figure 20. Schematic of the simple cross flow test problem.

Investigations are currently being performed to better understand the origin of the spatial oscillations. As the next step, one possible solution is to use an elemental-based approach, instead of the current nodal-based approach, to model the exchange of mass between the channels. Even though the cross flow model is not developed successfully, an attempt is made to capture its effects using an ad hoc engineering approach. This approach is discussed in details in the next section.

2.3.5. An Engineering Approach to Capture the Effects of Cross Flow with the SAM Core Channel Model

This section discusses the engineering approach implemented to the SAM core channel model to capture the effects of cross flow during the PLOFC accident. As discussed in Section 2.3.4, during a PLOFC, the existence of cross flow enhances mixing in the core, which helps distribute heat from the hotter inner core to the cooler outer core and to the side reflectors. As an attempt to capture the effects of enhanced heat loss from the inner core to the side reflectors, a `SurfaceCoupling` component is used to thermally couple the pebble heat structures in CH-1–CH-4 to the inner surface of the side reflector. The h_{gap} parameter in the `SurfaceCoupling` component, which dictates the rate of heat transfer between the coupled heat structures, is calculated using Equation 2 where the k_{eff} is calculated from the ZBS correlation shown in Equation 1.

Figure 23 compares the steady-state pebble surface temperature profiles of the core channel models with and without thermal coupling of individual channels to the reflector. As expected, no discernible differences

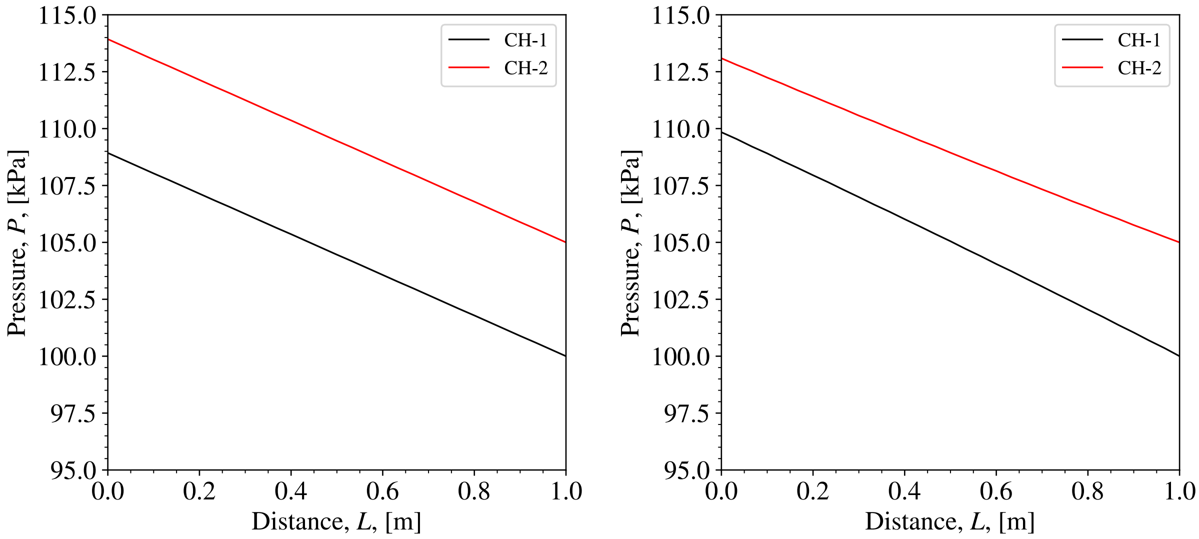

(a)

(b)

Figure 21. Comparison of the pressure profiles of the two channels (a) without the cross flow model and (b) with the cross flow model.

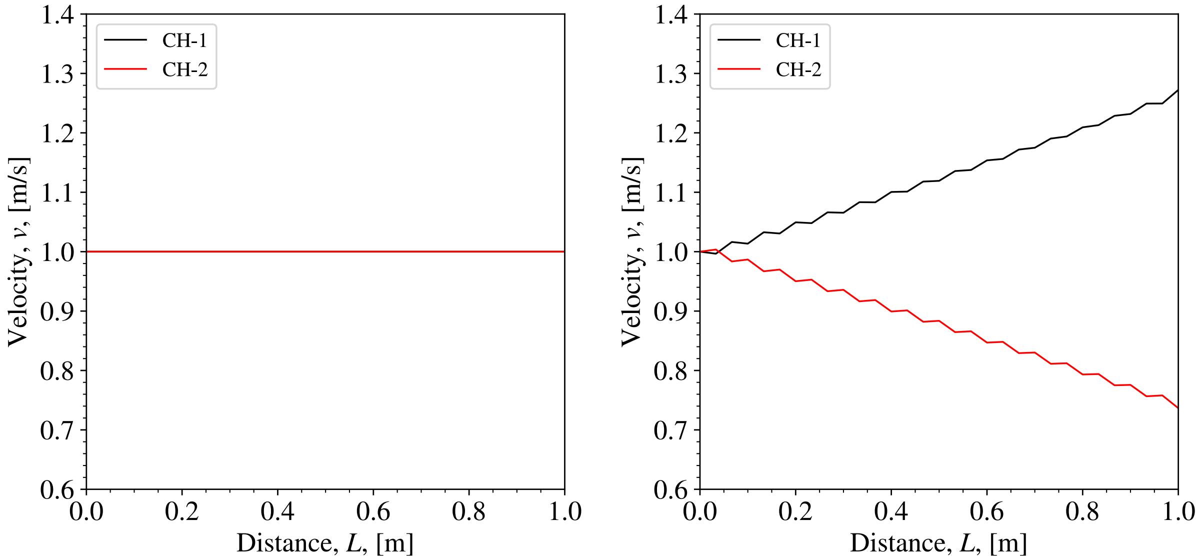

(a)

(b)

Figure 22. Comparison of the velocity profiles of the two channels (a) without the cross flow model and (b) with the cross flow model.

are observed between the two cases because heat generated in the core is removed predominantly by the flowing helium through forced convection.

With the heat structures in the individual channels thermally coupled to the side reflector, the PLOFC transient is simulated with the core channel model. The average and maximum pebble temperatures between the two core channel models are compared against the results from the 2D porous media model in Figure 24. With the individual channels coupled to the reflector, the updated core channel model predicts an overall lower

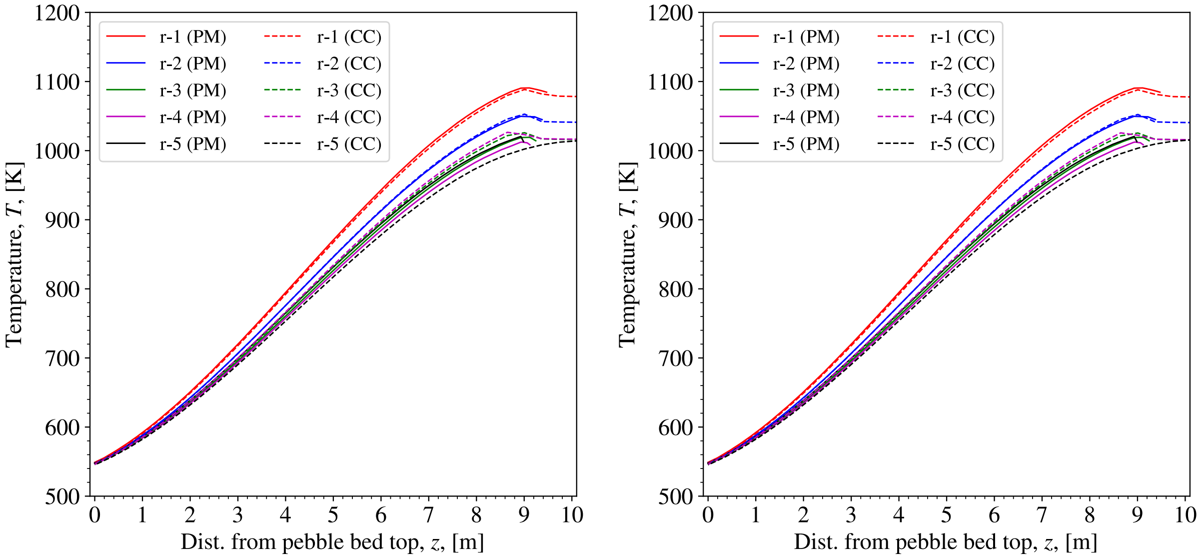

(a) (b)

Figure 23. Comparison of the steady-state pebble surface temperature profiles of the core channel models (a) with and (b) without thermal coupling of individual channels to the reflector.

pebble surface temperature due to enhanced decay heat removal from the core to the reflectors. The peak average temperature of the updated core channel model is about 1160 K while the peak average temperature of the original core channel model is about 1200 K. Similarly, the maximum pebble surface temperature is now much closer to that predicted by the 2D porous media model. With the updated model, the maximum pebble surface temperature is initially lower than the prediction from the 2D porous media model. However, the maximum temperature continues to increase and exceeds the result from the porous media model at about $t = 20$ hours. The updated core channel model predicts a peak temperature of about 1350 K, compared to the 1300 K from the 2D porous media model. On the other hand, the original core channel model shows a significant overprediction of about 1500 K.

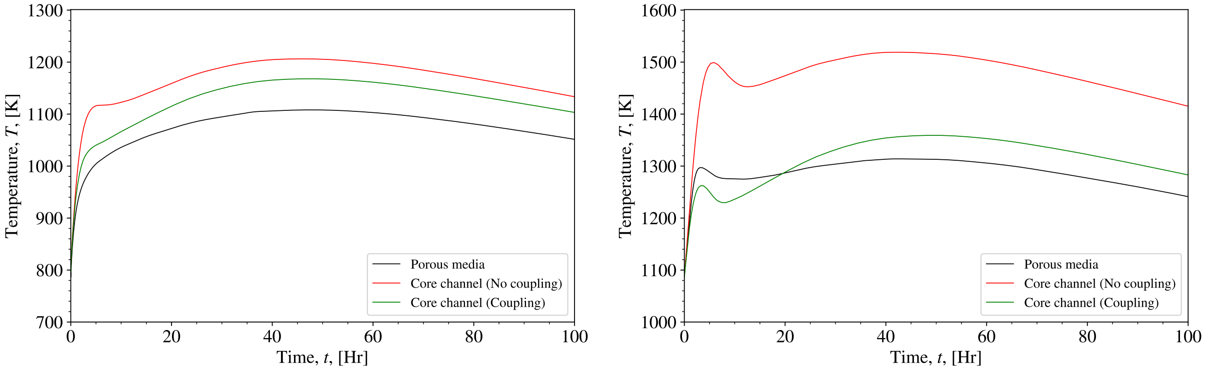

(a) (b)

Figure 24. Comparison of the PLOFC (a) average and (b) maximum pebble surface temperature of the core channel models with and without thermal coupling of individual channels to the reflector.

The analysis shows that by directly coupling the inner core channels to the reflectors, heat loss from the core can be enhanced and improve the prediction of the core channel model. In the future, more investigation will be performed to further improve the prediction of the core channel model. For example, the calculation of the h_{gap} term can be refined by considering convective effects. Sensitivity studies will also be performed to better understand the effects of h_{gap} on the decay heat removal rate of the core.

2.3.6. Variable Porosity at Near Wall Region with SAM Core Channel Model

So far, the SAM 1D core channel and 2D porous media models assume a uniform porosity of 0.39 in the core. However, near the wall, the presence of the wall causes the pebbles to pack in an orderly manner, lowering the packing fraction and altering the flow characteristics [26]. This effect is known as wall channeling, and it is an important phenomena for reactor designers, as it can cause flow to be diverted toward the outside of the core.

To capture the wall channeling effect, the SAM core channel model is modified to have a different porosity at the near wall region. As the first step, a simplified model is constructed as shown in Figure 25. The model consists of inlet and outlet plena, seven core channels, and a reflector with a temperature boundary condition on the outer surface. The two channels near the outer wall region have a width of 0.06 m, equivalent to the diameter of a pebble, while each of the inner channels has a width of 0.216 m. A uniform power density is assumed in the core. The porosities of the two outermost channels are calculated using the Cheng-Hsu correlation, which is one of the porosity correlations currently available in SAM [27].

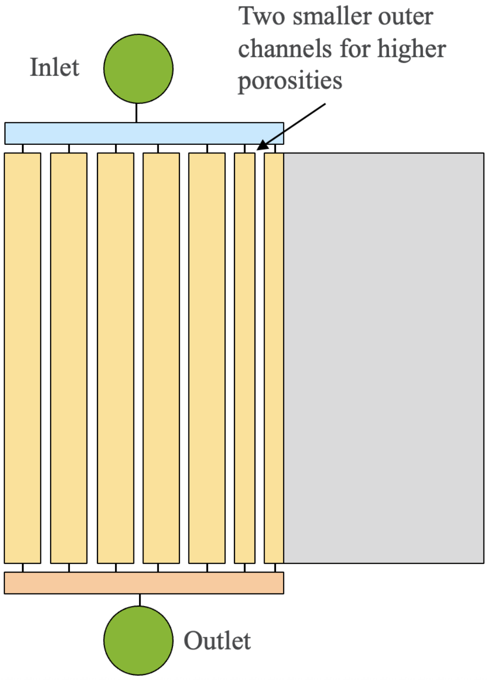

Figure 25. Schematic of the simplified core channel model for investigating the wall channeling effect.

The steady-state results from the simplified core channel model are summarized in Table 2. CH-6 and CH-7 have a porosity of 0.44 and 0.77, respectively, whereas the rest of the channels have a porosity of 0.39. The outlet fluid temperature of CH-7 is 530.4 K, which is significantly lower than the outlet temperatures of the other channels. This is due to a combination of low power fraction and high mass flow rate. For instance, CH-7 has a power fraction of 4.1%, which is slightly higher than that of CH-1 of 3.5%. However, the mass flow rate in CH-7 is more than 20× higher than the mass flow rate of CH-1. As a result, the pebble heat structures on CH-7 generate only a small amount of heat but the heat removal rate due to convection is much higher. Furthermore, the large mass flow rate enhances the convective heat loss from the fluid to the reflector wall. Consequently, this results in a significantly lower outlet temperature than the inner channels.

The simple analysis highlights several considerations for the use of the core channel model to capture the wall channeling effect. The channels near the wall must be sufficiently wide to avoid a significant jump in porosity from the inner core to the outer core that can result in an underprediction of the temperature at the outer core.

Table 2. Summary of the steady-state results from the simplified SAM core channel model with variable porosity at the near wall region.

Channels	Porosity [—]	Flow Area [m^2]	Power Fraction [—]	Outlet Temperature [K]	Outlet Velocity [m/s]	Mass Flow [kg/s]
1	0.39	0.0572	0.035	1357.2	12.88	1.56
2	0.39	0.1715	0.104	1357.2	12.88	4.68
3	0.39	0.2858	0.174	1357.2	12.88	7.80
4	0.39	0.4001	0.243	1356.9	12.88	10.92
5	0.39	0.5145	0.312	1347.9	12.82	14.06
6	0.44	0.1841	0.091	1011.5	12.13	6.33
7	0.77	0.3352	0.041	530.4	18.48	33.25

Based on the lessons learned from the analysis above, the full GPBR200 core channel model is used to capture the wall channeling effect. At the same time, the 2D porous media model is also modified for the same purpose. The Hunt-Tien correlation is used to calculate the porosity in the core [27], which is done internally by SAM in the 2D porous media model. The radial distribution of the porosity in the 2D model is shown in Figure 26. In the outermost element, which has a width of 0.15 m, the porosity is 0.404 while the remaining of the core has a porosity of 0.39. In the SAM 2D porous media model, porosity is treated as an `AuxVariable` of the `constant` type. This means that the porosity of each cell is taken as an average constant value with no distribution within the cell.

Meanwhile, for the core channel model, the core is modeled with the same five channels from previous discussions, instead of seven as in the simplified model. This is due to the restrictions of channel sizes near the outer wall learned from the simplified model discussed earlier. In this model, CH-5 has a width of 0.21 m. CH-1–CH-4 have a porosity of 0.39, whereas CH-5 is given a porosity of 0.4, which is the average value calculated from the 2D porous media model from $r = 0.99$ m to 1.2 m. A nonuniform power density distribution based on the work by Stewart et al. [18] is applied to both the 2D porous media and core channel models.

The steady-state comparisons of the pebble surface temperature, fluid temperature, and velocity are shown in Figure 27. Overall, good agreements are observed between the core channel model and the porous media model. However, near the wall, the core channel model shows a slightly lower pebble and fluid temperature. This is likely because the core channel model shows a higher velocity near the wall than the porous media model, especially at the upper half of the core.

Next, the PLOFC accident is modeled with both models. The average and maximum pebble surface temperatures are shown in Figure 28. This model shows that the core channel model still predicts higher pebble temperatures than the porous media model. However, considering variable porosity at the near wall region, the agreement between the two models slightly improves. This is evident in the maximum pebble surface temperature where the agreement of the first peak between the two models is closer than that in Figure 24. The RCCS decay heat removal rates from both models are compared in Figure 28 and are close to each other. The core channel model shows a slightly higher decay heat removal rate, but the overall trend compares well with the result from the porous media model. In both models, the heat removal rate overtakes

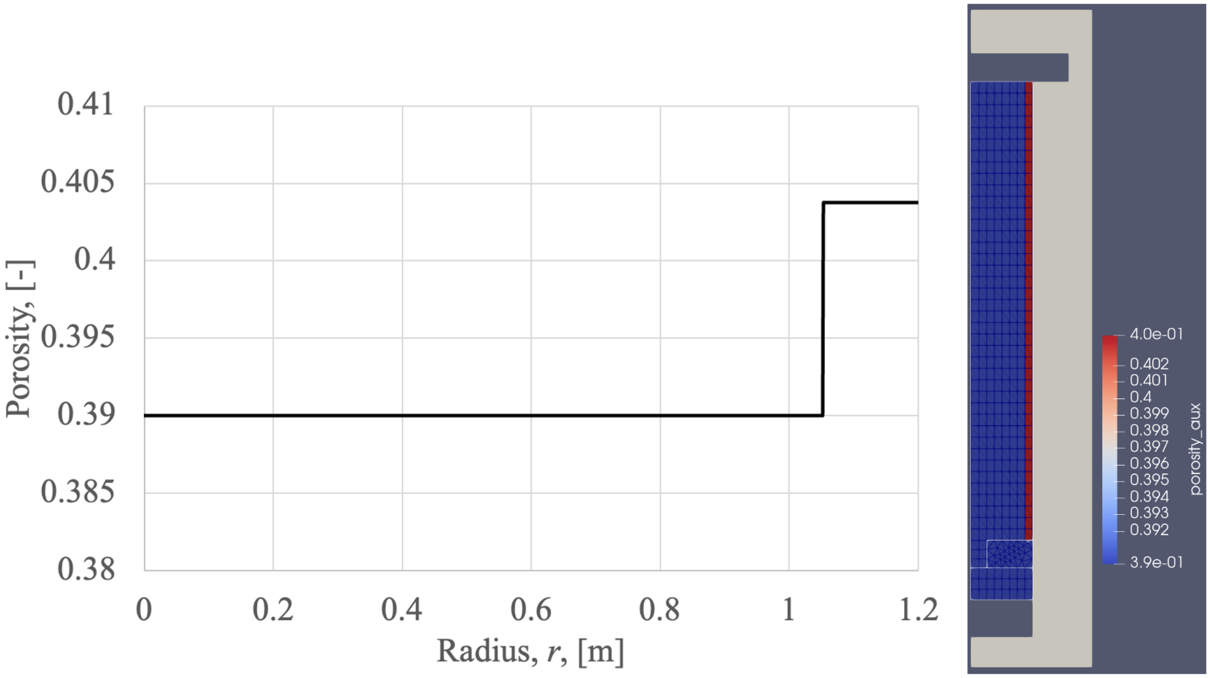

Figure 26. Radial distribution of the porosity in the 2D porous media model.

the decay heat at around t = 50 hours, at which point the pebble temperature peaks and starts to decrease.

To better understand the wall channeling effects, the results from the 2D porous media model with uniform and variable porosities are compared. The mean and maximum pebble surface temperatures between the two 2D porous media models are compared in Figure 30. The pebble temperature predicted by the uniform porosity model is overall lower than the variable porosity model. During the initial stage of the transient, the results from both models show good agreement. The models start to diverge after about 20 hours from the beginning of the transient where the variable porosity model predicts a higher average pebble surface temperature than the uniform porosity model. This is likely because the lower porosity near the wall causes more flow into the near wall region instead of the hotter inner core region. The decay heat removal rate from both models are compared in Figure 31. The decay heat removal rates from both models are similar, but the uniform porosity model shows a slightly lower value due to a lower temperature.

Figure 32 shows the temperature difference between the two 2D porous media models during the PLOFC, where the temperature difference is defined as $\Delta T = T_{uniform} - T_{porous}$. During the steady state, the temperature outside of the core between the two models is largely the same, whereas in the core, the variable porosity model shows a higher temperature at the inner core but a lower temperature near the wall. This is because the variable porosity model has a lower flow through the inner core and a higher flow near the wall as the porosity is higher near the wall. In the first 24 hours of the transient, the core of the uniform porosity model consistently shows a higher temperature. At t = 52 hours where the maximum pebble temperature reaches its peak, the opposite trend starts to emerge where the variable porosity model starts to show a higher temperature in the core than the uniform porosity model. As the transient progresses, the temperature difference between the two models continues to increase. This is also evident in the mean and maximum pebble temperatures shown in Figure 30.

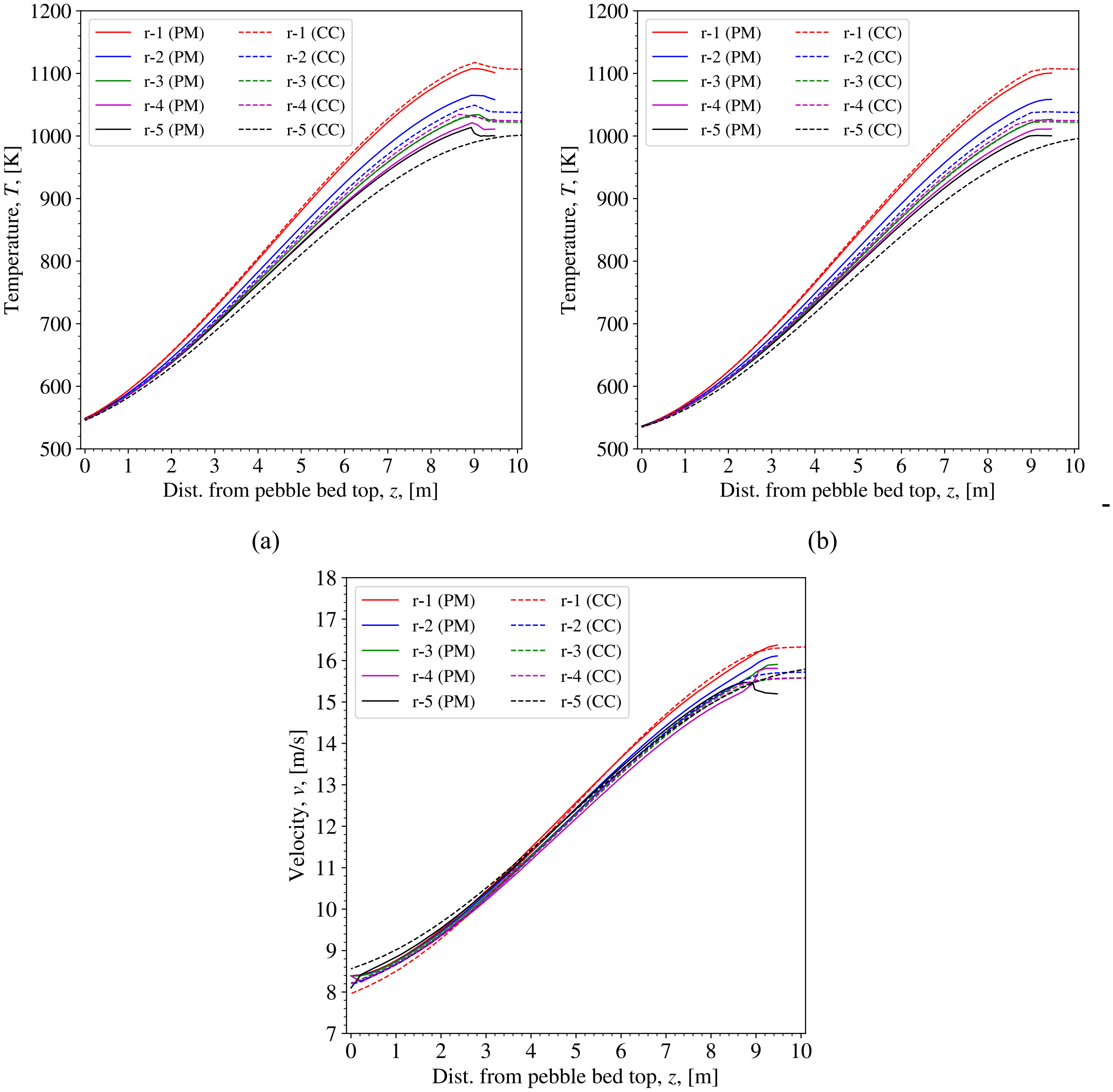

(a)

(b)

(c)

Figure 27. Comparison of the PLOFC (a) average and (b) maximum pebble surface temperature of the core channel models with and without thermal coupling of individual channels to the reflector.

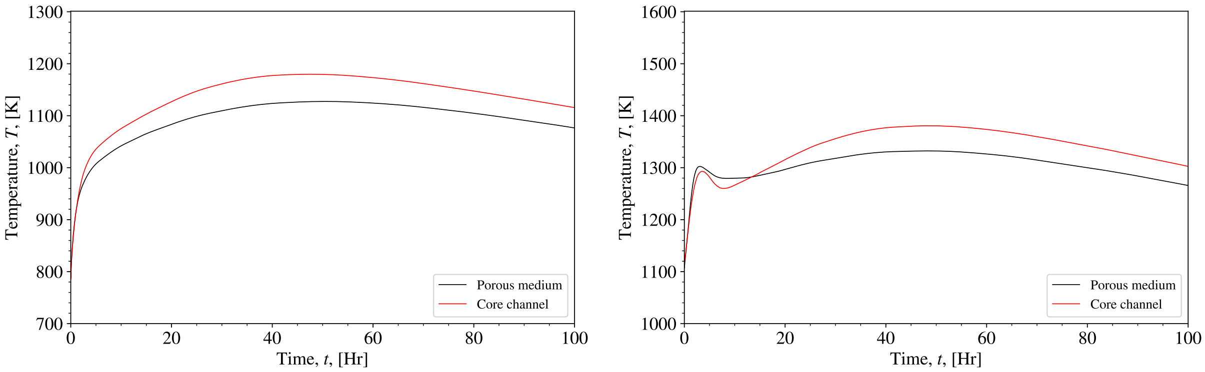

(a) (b)

Figure 28. Comparison of the PLOFC (a) average and (b) maximum pebble surface temperature of the core channel and 2D porous media models with variable porosity at the near wall region.

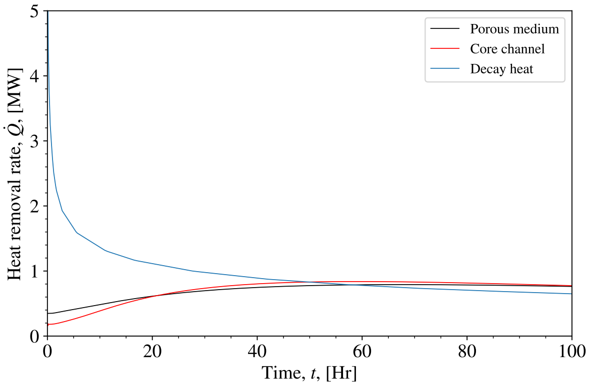

Figure 29. Comparison of the decay heat removal rate of the core channel and 2D porous media models with variable porosity at the near wall region.

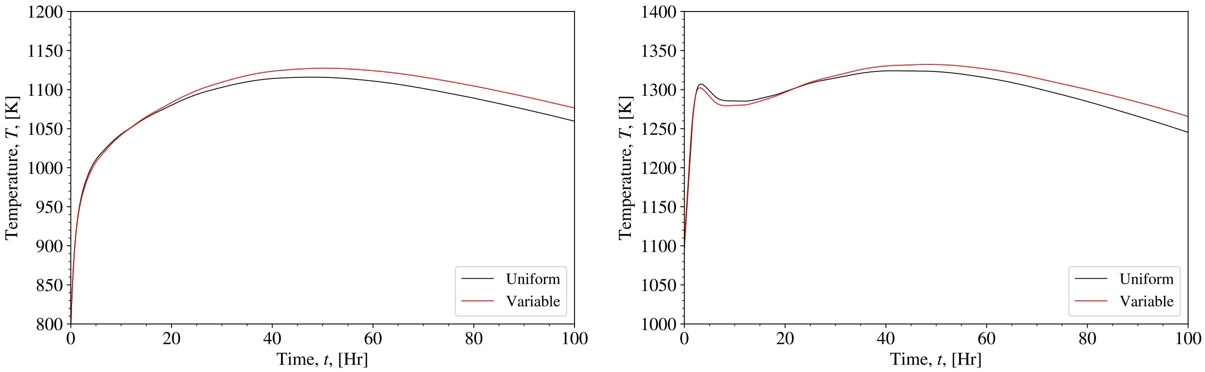

(a) (b)

Figure 30. Comparison of the PLOFC (a) average and (b) maximum pebble surface temperature between the 2D porous media models with uniform and variable porosities.

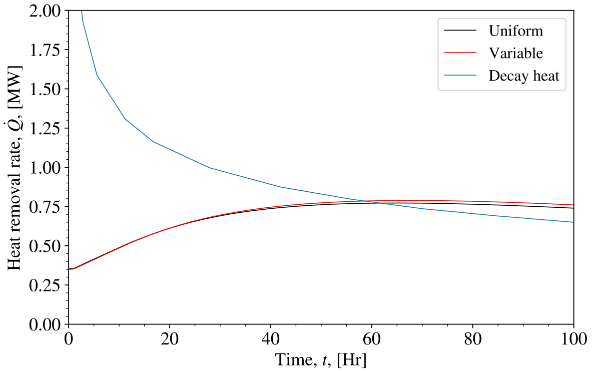

Figure 31. Comparison of the decay heat removal rate of the 2D porous media models with uniform and variable porosities at the near wall region.

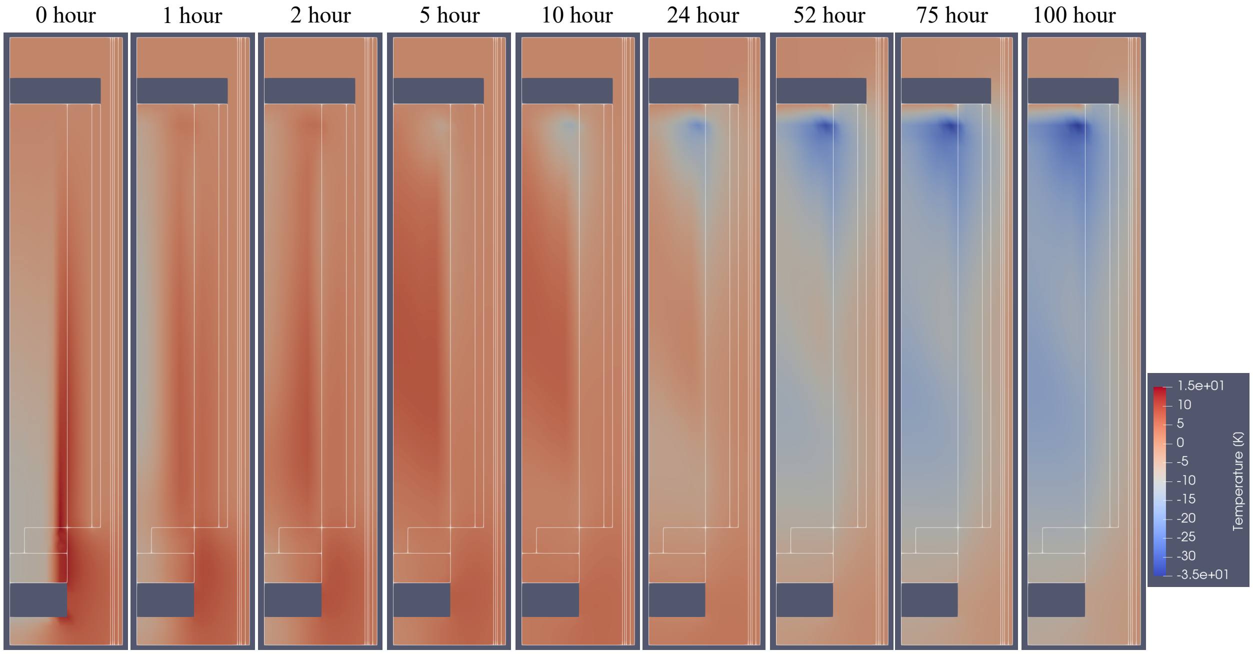

Figure 32. Temperature difference between the 2D porous media models with uniform and variable porosity during the PLOFC, where $\Delta T = T_{uniform} - T_{porous}$.

2.3.7. Preliminary Evaluation of the Online Cross-Section Generation Capability

This section describes the Griffin-SAM coupled calculation using the online cross-section generation capability for the steady-state GPBR200 core. The coupling scheme, data transfer strategy, energy conservation approach, and results are presented in that order.

Figure 33 illustrates the coupling scheme implemented using the `MultiApps` system in MOOSE, where Griffin serves as the main application and SAM as the subapplication. Since a diffusion or transport solver always requires cross sections, the online cross-section generation module is executed at `TIMESTEP_BEGIN`. For cross-section generation, temperature and density variables are averaged over cross-section regions defined by `region_id` in the mesh, and the averaged values are used to generate pebble cross sections. In this work, each subdomain is defined by a 2-by-2 element block and is treated as a cross-section region. The online cross-section generation module accepts three temperatures: (1) TRISO kernel temperature, (2) moderator temperature (representing TRISO particle layers, the surrounding matrix, and the graphite shell of the pebble), and (3) coolant temperature. In this study, a single effective solid temperature within each pebble was used to represent all three temperatures.

For flux calculations, a diffusion calculation was performed using homogenized cross sections for pebbles and coolant obtained with flux weighting in a 70-group energy structure. Following the diffusion calculation, power was evaluated by multiplying the scalar flux by the kappa-fission cross section. The `[PowerDensity]` block in Griffin reports the power produced per mesh volume (which includes both pebble and coolant regions), whereas SAM requires power density per fuel-zone volume. The fuel zone corresponds to the graphite sphere of radius 2.5 cm in which TRISO particles are dispersed. Accordingly, the power density was scaled by the ratio of the mesh volume to the fuel-zone volume before being transferred to SAM.

Using the transferred volumetric heat source, a SAM pseudo-transient calculation was performed for a simulation time of 100,000 seconds, which was sufficient to obtain a steady-state solution. The relative and absolute tolerances for the nonlinear iteration were set to 10^{-7} and 10^{-5}, respectively. A 1D core channel model with five channels was employed. In each channel, spherical 1D heat conduction in a homogeneous pebble (using effective thermal conductivity) and 1D porous media flow with conjugate heat transfer were solved to update the effective solid temperature. Once the temperature converged, it was transferred back to Griffin and used to update cross sections in the next Picard iteration.

The Picard iteration continued until either (1) the absolute value of the residual norm of the neutronics solution fell below 10^{-7}, or (2) the ratio of the residual norm at the current iteration to that at the initial stage fell below 10^{-5}. The residual norm is determined as the bigger value between ones evaluated before and after the diffusion solve. Since the one evaluated before the diffusion solve, $|R|_{\mathrm{B}}$, is based on the new cross-section set from the updated temperature and the other, $|R|_{\mathrm{E}}$, is already a converged quantity after solve, $|R|_{\mathrm{B}}$ is always bigger than $|R|_{\mathrm{E}}$. Therefore, the residual norm for the convergence check is practically $|R|_{\mathrm{B}}$. Since there is no `MultiApps` coupling at `TIMESTEP_BEGIN`, residual is not evaluated at `TIMESTEP_BEGIN` by default. To force the evaluation of $|R|_{\mathrm{B}}$, `fixed_point_force_norms` needs to be turned on. For this problem, six Picard iterations were required to satisfy the convergence criteria.

For energy conservation, the `MultiAppConservativeTransfer` method was employed. This transfer method normalizes the variable such that the integrated value of the transferred variable matches that of the source variable. By specifying `PostProcessors` for the integrated power density (i.e., the total energy produced) for each channel in Griffin and SAM in the transfer, the total per-channel energy calculated in Griffin can be exactly conserved in SAM. To enable this normalization process, the SAM code was updated to initialize the volumetric heat source variable with a nonzero value. By default, this variable is reset to zero at the beginning of each Picard iteration, and if its integrated value is zero, the transfer routine skips the normalization. Although `FullSolveMultiApp` provides an input parameter, `keep_solution_during_restore`, to prevent variable reinitialization in each Picard iteration, this option applies only to system variables and not to `AuxVariables`.

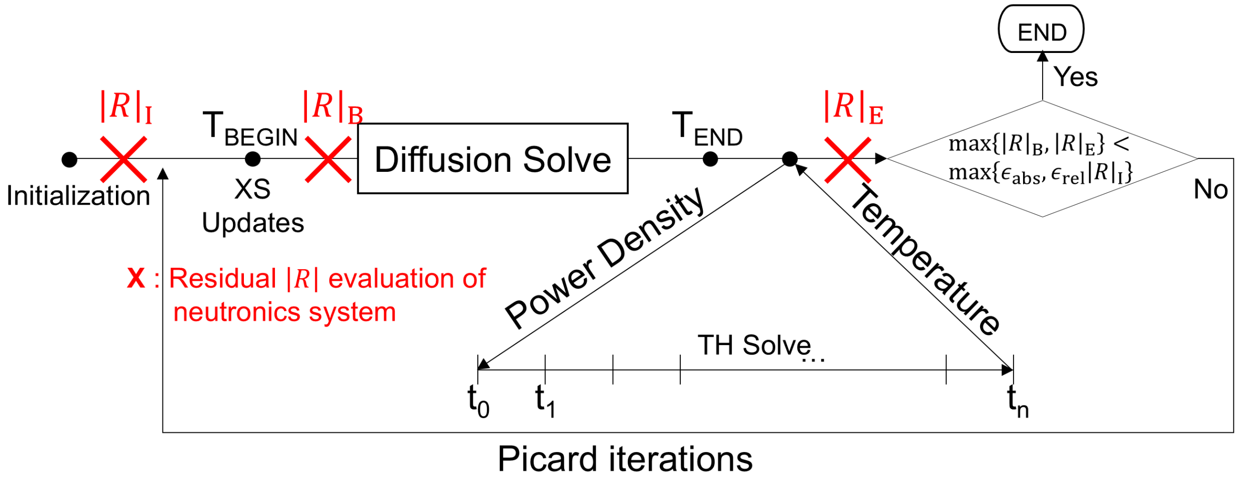

Figure 33. Griffin-SAM coupling scheme with the online cross-section capability.

For data transfer, `MultiAppGeneralFieldNearestLocationTransfer` was employed to exchange power density and temperature variables between Griffin and SAM. Figure 34 illustrates the transfer scheme. The red dots represent the nodes of the axial 1D elements for each vertical channel in the SAM mesh, while the green dots denote the centroids of elements in the Griffin mesh. Each channel spans two radial elements in the Griffin mesh, and the green dashed boxes indicate the physical volumes occupied by each channel.

For power density transfer, the `Transfer` specifies the source blocks in Griffin from which the variable is obtained, as well as the target blocks in SAM that receive the value. This ensures that data are exchanged between corresponding channels. As illustrated in the left figure of Figure 34, however, the nearest location transfer has potential issues that require future improvement. First, elements in the second radial column of each channel do not participate in the transfer, since the elements in the first column are always nearest to the SAM nodes. This might not be causing noticeable error due to normalization to conserve energy per channel. However, if necessary, this can be improved by introducing a separate variable that stores the average value across the two radial elements and transferring that value instead. Second, multiple axial nodes in SAM sometimes receive values from the same element centroid in Griffin. This limitation could be mitigated by adopting a different transfer method, such as geometric interpolation transfer.

Temperatures at element centroids in Griffin are transferred from the nearest nodes in SAM, as illustrated in the right panel of Figure 34. For comparison, a temperature value at a specific spatial location is taken from the representative average value of the corresponding channel, whereas a power density value for the representative average pebble is taken from the value at a specific spatial location. Because the former approach is more consistent than the latter, the temperature transfer using the nearest node transfer poses relatively fewer issues than the power transfer.

Figure 35 shows the change in the eigenvalue and the decrease of the relative residual norm over Picard iterations. The simulation terminated after the sixth Picard iteration when the relative residual norm fell below 10^{-7}. The evolution of the eigenvalue is explained by Figure 36, which shows the temperature change over iterations. The initial eigenvalue, $k = 1.35939$ at Iteration 1, was evaluated under the isothermal 900 K condition at Iteration 0. As the average temperatures of all five channels fell below 900 K, temperature feedback increased the eigenvalue to 1.36963, which in turn raised temperatures; as the temperatures rose, the eigenvalue decreased to 1.36364. Beyond this point, the temperature field was nearly converged (within ± 2.5 K of the final values, see Figure 37), so the neutronics solution stabilized and fully converged over the next three iterations. Figures 37 and 38 show the absolute differences in the temperature and power distributions with respect to their converged values at each iteration. The converged power is top-skewed because the

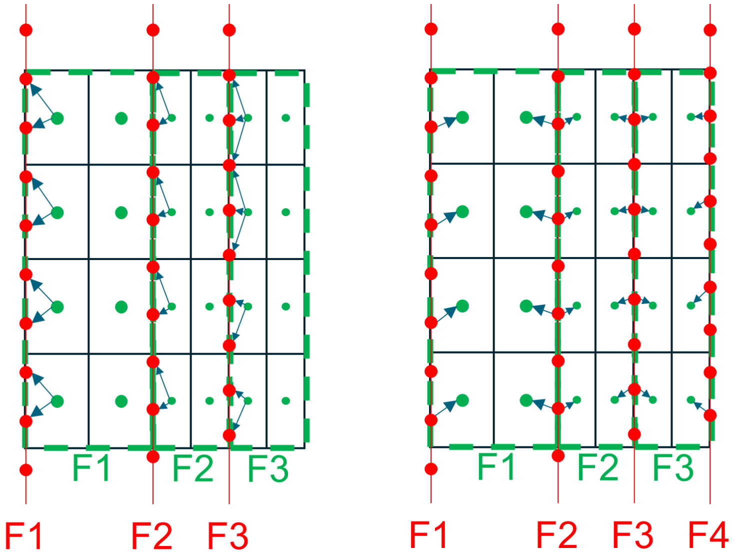

Figure 34. Nearest location transfer of power (left) and temperature (right) variables.

upper region is cooler. These differences diminish with each iteration, and by Iteration 5, they are negligible, indicating convergence.

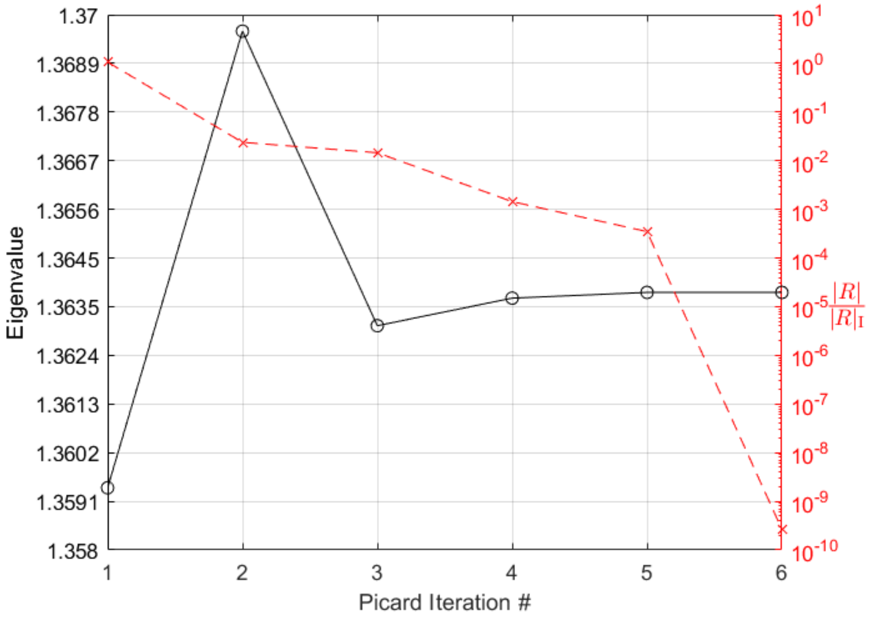

Figure 35. Evolution of eigenvalue and residual norm over Picard iterations.

Although not shown in the figures, the SAM `PostProcessors` confirmed that the power transferred to SAM was conserved on a per-channel basis at each iteration. However, the total heat removal rate was approximately 5% lower than the total core power of 200 MW, owing to heat losses from the core to the surroundings.

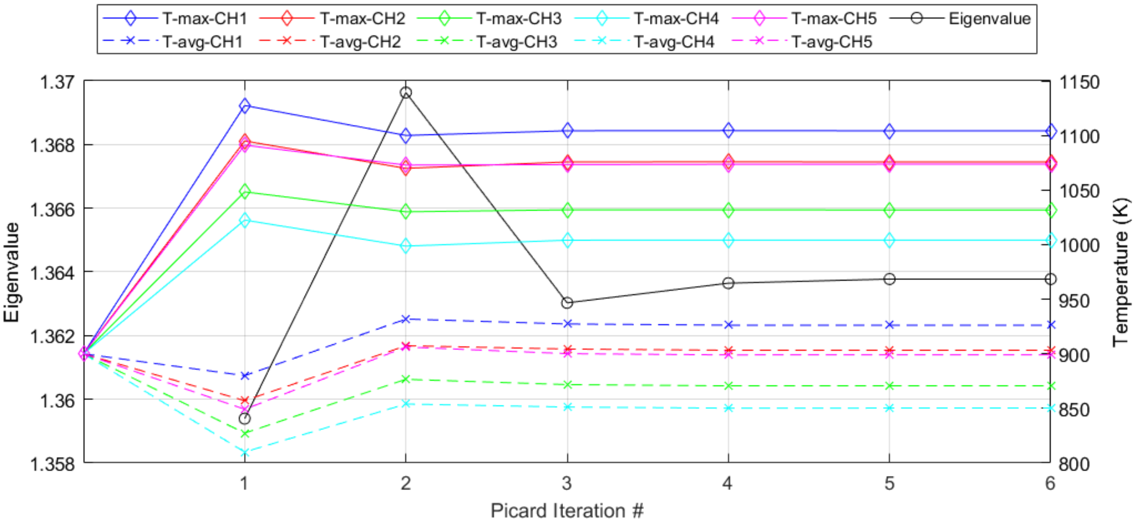

Figure 36. Evolution of eigenvalue and channel-wise temperatures over Picard iterations.

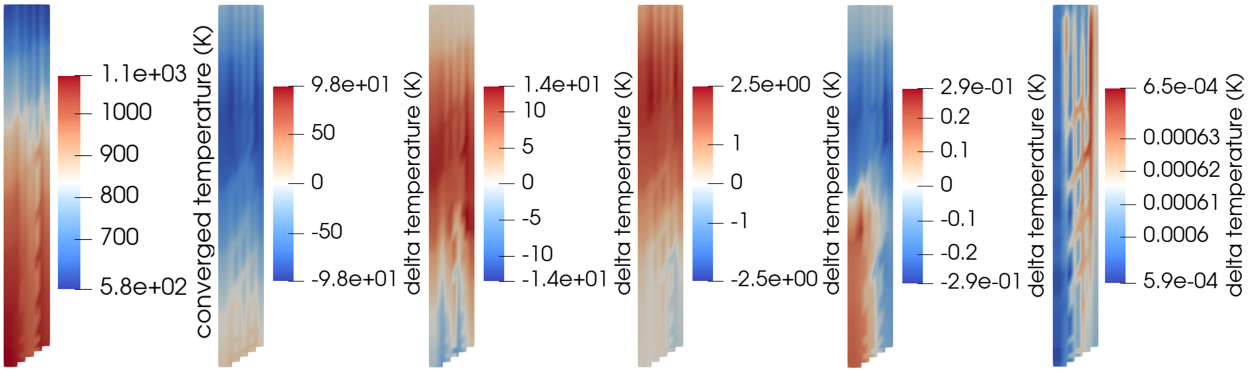

$T^{(6)}$ $T^{(1)} - T^{(6)}$ $T^{(2)} - T^{(6)}$ $T^{(3)} - T^{(6)}$ $T^{(4)} - T^{(6)}$ $T^{(5)} - T^{(6)}$

Figure 37. Evolution of temperature distribution error over Picard iterations. Superscript (l) means l'th Picard iteration.

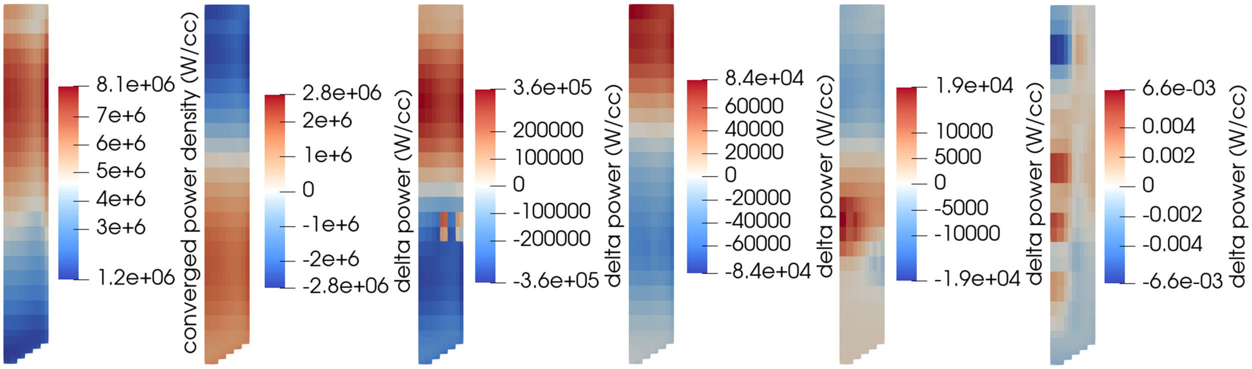

$P^{(6)}$ $P^{(1)} - P^{(6)}$ $P^{(2)} - P^{(6)}$ $P^{(3)} - P^{(6)}$ $P^{(4)} - P^{(6)}$ $P^{(5)} - P^{(6)}$

Figure 38. Evolution of power distribution error over Picard iterations. Superscript (l) means l'th Picard iteration.

3. PRISMATIC HTGR APPLICATIONS/HTTF BENCHMARK

The HTTF [28] is an integral effects test facility at Oregon State University (OSU) being used as the basis for the Organisation for Economic Co-operation and Development/Nuclear Energy Agency (OECD/NEA) thermal-hydraulic code validation benchmark for an HTGR. This benchmark, described in Reference [29], provides three problems: Problem 1 for hot gas mixing in the lower plenum, Problem 2 for a depressurized conduction cooldown (DCC) transient [30], and Problem 3 for a pressurized conduction cooldown (PCC) transient. Each problem in the benchmark includes code-to-code comparisons in Exercise 1 and code-to-data comparisons in Exercise 2. Problem 3, Exercise 1 is broken down into four subexercises: 1A to simulate a full-power steady state; 1B to simulate a PCC from full power; 1C for a low-power steady state using the heating profile in Test PG-27 [31]; and 1D to simulate a low-power PCC. Code-to-code comparisons for Exercises 1A and 1B have been published previously [32]. Table 3 shows the matrix of exercises and problems and indicates which tools are used for each combination: System codes (SYS), computational fluid dynamics (CFD) codes, and system-to-CFD code couplings (COU). This report covers Exercise 1 of Problem 1 and Exercises 1C, 1D, and Exercise 2 of Problem 3.

Table 3. Benchmark exercises and problems.

	Exercise 1	**Exercise 2**	**Exercise 3**
	Fixed boundary condition	**Open boundary condition**	**Error scaling**
Problem 1 lower plenum	CFD	CFD	n/a
Problem 2 DCC	SYS/COU	SYS/COU	SYS
Problem 3 PCC	SYS/COU	SYS/COU	SYS

3.1. The High Temperature Test Facility

The HTTF is an integral helium-cooled test facility located at OSU. It was based on General Atomic's MHTGR design, which uses prismatic graphite blocks in the core and reflectors. Compared to the MHTGR, the HTTF was scaled to one-fourth the size in length and diameter and operated at a prototypical temperature but at reduced pressure. The HTTF was primarily designed to model DCC transients therefore the reduced pressure is not a factor. Figure 39(a) shows the RPV with flow path of helium coolant in normal operation. The RPV is surrounded by a RCCS constructed of water-cooled panels to establish boundary conditions for the tests and control radiation heat transfer from the RPV wall. The cavity between the RPV and RCCS panels is not air tight, and it is expected that air flow through the cavity removes some amount of heat from the RPV.

The core is made up of 10 Greencast 94-F ceramic blocks, shown in Figure 39b, three lower reflector and two upper reflector blocks. In the radial direction, the core is divided into regions: central reflector, inner/middle/outer core, outer reflector, and side (permanent) reflector. In the axial direction, the blocks are stacked upon one another as shown in Figure 39c. Also, illustrated in Figure 39b are 558 coolant channels cast in the ceramic blocks through which helium coolant flows to remove heat. The core is electrically heated by 210 graphite heater rods (orange circles in Figure 39b). The HTTF has over 400 data acquisition channels for thermocouples, pressure transducers, and gas sensors.

3.2. Problem 1---Exercise 1: Fixed Boundary Conditions

3.2.1. Overview of Lower Plenum Mixing Problem

Among the identified safety-relevant phenomena for the gas-cooled reactors, the outlet plenum flow distribution was ranked as high importance with a low knowledge level in the phenomenon identification

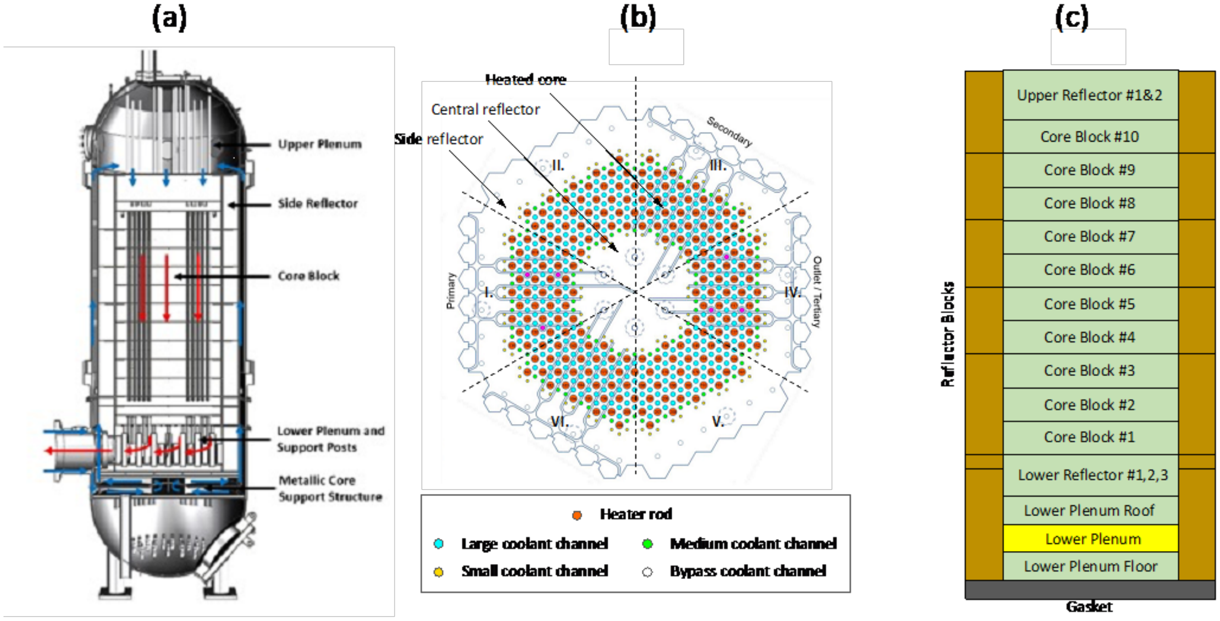

Figure 39. (a) RPV with flow path; (b) core block; (c) axial block stack.

and ranking table [33]. In the HTTF, heated coolant from the core region enters the lower plenum—also referred to as the core outlet plenum—through 234 narrow channels, each 1 inch (2.54 cm) in diameter. These channels cause the jetting of the helium gas flow into the plenum. Because the jets originated from different regions in the core, they have nonuniform temperatures, which risk yielding high cycling thermal stresses in the lower plenum, negative pressure gradients opposing the flow ingress, and hot streaking.

The lower plenum geometry, illustrated in Figure 40, consists of 163 ceramic cylindrical posts that support the core structure. It is enclosed by the lower side reflectors, the lower plenum floor, and the lower plenum roof, with an internal height of 22.2 cm. The helium jets enter from the vertical coolant channels in the core and exit through a cylindrical horizontal hot duct, which serves as the outlet channel.

These complex jet-to-crossflow interactions and resulting temperature fluctuations cannot accurately be captured by 1D system codes. Instead, higher fidelity CFD models are required to predict the detailed thermal and flow behavior in the HTTF lower plenum.

3.2.2. CFD Results

The Argonne National Laboratory team employs the CFD code, NekRS, to simulate the flow mixing problem in the HTTF lower plenum with the two-equation k-τ turbulence model. NekRS is a spectral element CFD code, designed for optimized efficiency on GPUs, developed as part of the U.S. DOE NEAMS program. NekRS and its predecessor Nek5000 have a long history of applications in reactor thermal hydraulics [34]. The $k - \tau$ model [35], as a variant of the $k - \omega$ model, is selected here due to its robustness and flexibility in wall boundary condition specifications. A computational grid consisting of a tetrahedra and wedge cells was first created with ANSYS Mesh and then converted into a pure hexahedra mesh using a native tet-to-hex Nek5000 utility [36]. The resulting mesh has 3.8 million cells, and the total degrees of freedom is approximately 102.1 million in the NekRS simulations with a polynomial order of 3. Due to the complexity of the lower plenum CAD model, generating a very-high-quality boundary-layer mesh near wall surfaces is challenging, and the first grid layer is generally positioned at y+ values on the order of 1.

The CFD simulation was carried out over a period of 20 convective time units to ensure the development

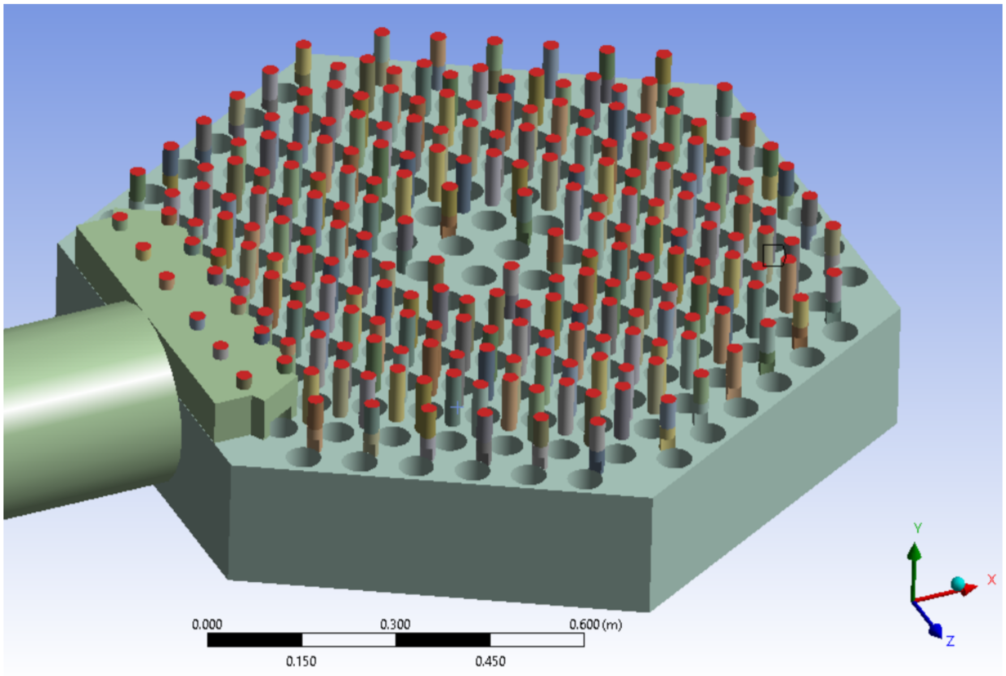

Figure 40. The HTTF lower plenum CAD model (inlets highlighted in red).

of a fully turbulent flow field. A convective time unit corresponds to the time required for the mean flow to traverse one hydraulic diameter within the hot duct. Given the use of an unsteady RANS turbulence model and then expected Reynolds number of approximately 99,039 at the hot (horizontal) duct, achieving a fully steady state is not feasible; however, a quasi steady state was achieved, allowing for the extraction of time-averaged flow statistics. The velocity distribution, as shown in Figure 41, reveals a progressive increase in velocity magnitude as the flow advances toward the hot duct, with distinct recirculation zones forming behind the lower plenum posts. Further analysis of the velocity and temperature distributions along the centerlines of the lower plenum and hot duct (Figure 42) highlights a notable acceleration of the flow at the junction between the lower plenum and the hot duct, followed by a slight decrease near the duct exit. A local velocity peak is observed in the region where flow interacts with rakes installed in the hot duct. Downstream of $x/D_h \approx -2$, significant velocity fluctuations suggest the presence of flow separation and recirculation. In terms of thermal behavior, the temperature remains relatively uniform across the bulk of the lower plenum but shows a high level of fluctuations in the peripheral regions. The temperature evolution downstream of $x/D_h \approx -2$ may indicate potential thermal stratification within the hot duct. In summary, the flow within the lower plenum exhibits pronounced local acceleration, recirculation, and interactions with constraining structures, resulting in sustained velocity and temperature fluctuations downstream. The peripheral temperature variations and downstream stratification patterns point to complex thermal-hydraulic behavior that could impact the long-term operational safety of the system.

3.3. Problem 3---Exercise 1: Code-to-Code Comparison

Table 4 lists the six participants from five countries and the system codes that were used to perform simulations for Problem 3.

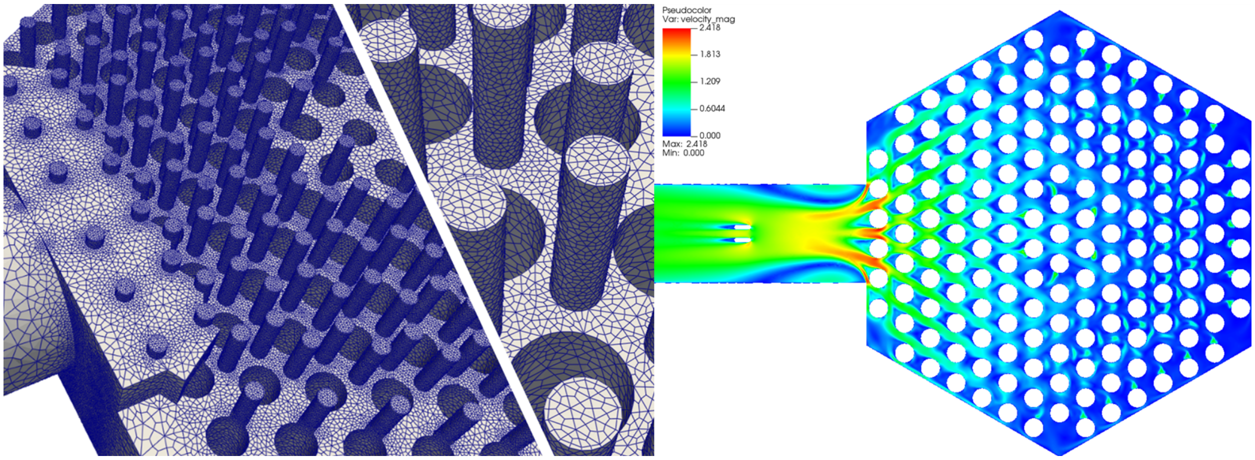

Figure 41. Computational grid of the HTTF lower plenum (left) and the time-averaged nondimensional velocity field (right).

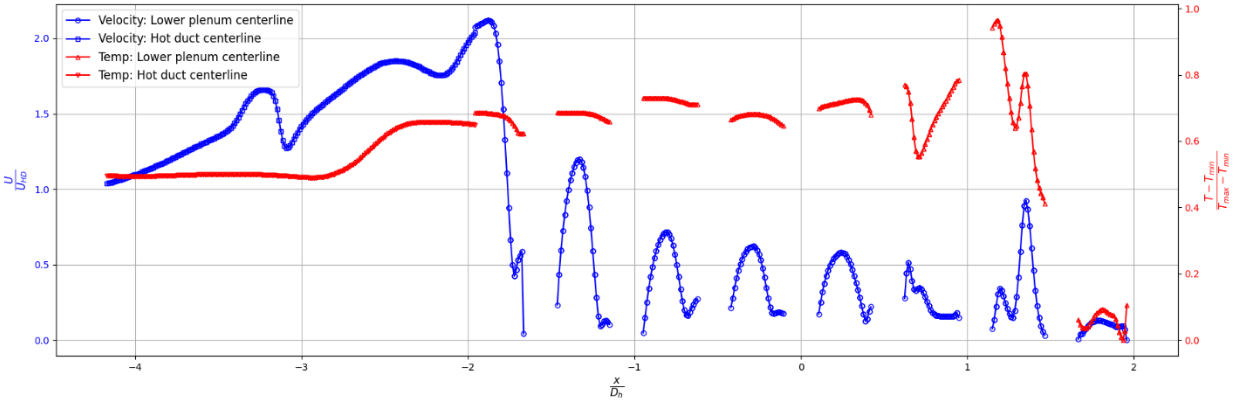

Figure 42. Time-averaged velocity and temperature profiles along the lower plenum and hot duct centerlines from NekRS simulations.

3.3.1. Description of Problem 3 Exercises 1C and 1D

These exercises utilize the heating condition in HTTF Test PG-27, which operated at a low power and pressure. Only 2 of 10 heater banks, or 42 out of 210 heater rods, were active, producing 86 kW in a steady-state condition. The electric circuits that connect the active rods form a zig-zag pattern, as shown in Figure 43a. The heat-up process took more than 2 days to establish a quasi steady-state condition. For simulating this problem, it is more convenient to disregard the heat-up period and only consider the steady-state condition within the time interval between 200,000 and 249,500 seconds in Figure 43b. Table 5 summarizes the operating and boundary conditions for Exercise 1C. Exercise 1D simulates a PCC assuming forced flow is terminated in 1 second. In the beginning of the transient, heating power is increased for 3 minutes before decreasing, as shown in Figure 43b. The RCCS continues to operate normally. Simulations are performed for 48 hours.

3.3.2. Steady-State Results

Table 6 tabulates the flow distribution in the inner and outer reflector and the core regions as calculated by the six models. In this report, the INL results are designated as RELAP5 while the Canadian Nuclear

Table 4. Participants and system codes used in Problem 3.

Participant Institution	Country	System Code
Argonne National Laboratory	United States	SAM
Idaho National Laboratory (INL)	Uited States	RELAP5
Korean Atomic Energy Research Institute	South Korea	GAMMA+
Nuclear Research Consultancy Group	The Netherlands	SPECTRA
Canadian Nuclear Laboratory	Canada	RELAP5
HUN-REN Centre for Energy Research/ Budapest University of Technology	Hungary	CATHARE

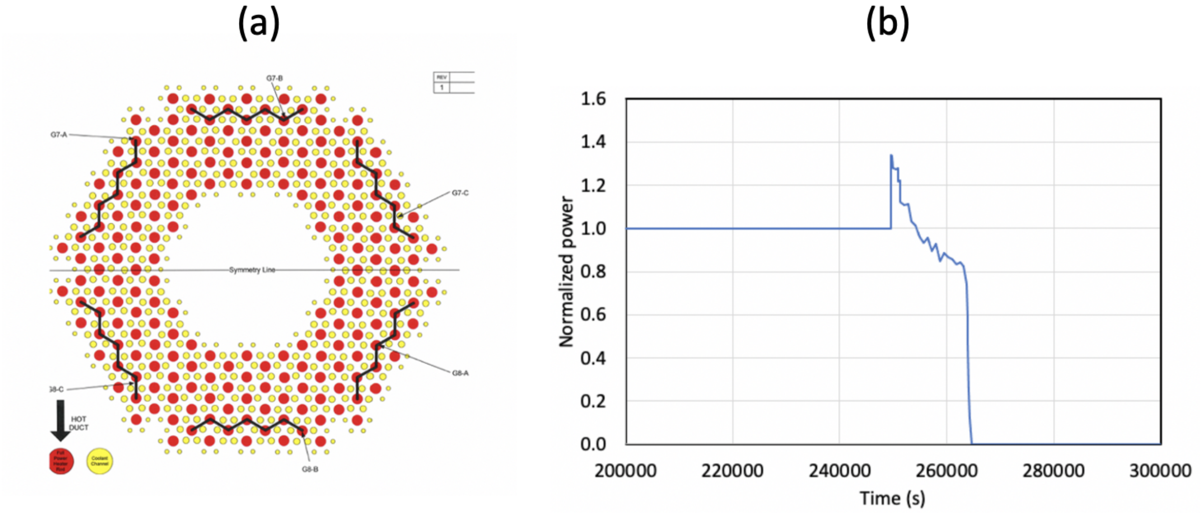

Figure 43. (a) Active heater rods connected by black lines and (b) heating power profile.

Laboratory results are designated as CNL-RELAP5. Because the core is not uniformly heated, some models redistribute the number of coolant channels in the core to align with their modeling approach. Nevertheless, the agreement among the different models is reasonable.

Figure 44 compares the helium temperature in the coolant channels across the core block from the inner reflector (R ~ 0.1) to the outer reflector (R ~0.55) for Block 1 and Block 9. All models predict a right-skewed radial temperature profile because the active heater rods are located in the vicinity of the middle/outer core. As expected, the temperature in Block 1 (bottom-heated block) is higher than that in Block 9 (by about 150 K) as helium flows from top to bottom. Apart from this consistent trend, there are notable differences in the results of the five models. The peak temperature predicted by the CNL-RELAP5 and CATHARE models are higher than the other models by ~100 K. In the inner reflector and inner core region, the SPECTRA temperature is~50 K higher than all other models while the CNL-RELAP5 models predicts the lowest temperature. In Block 1 (but not in Block 9), SAM agrees reasonably well with RELAP5 as does GAMMA+ with CATHARE.

Table 7 tabulates the heat loss from the reactor vessel, which is removed in the RCCS in two modes. A large fraction of the heat loss is removed by thermal radiation from the vessel to the RCCS panels, which are cooled by water, and a smaller fraction is removed by the convection of air flowing through the RCCS cavity, which is the space between the reactor vessel and the RCCS panels. The total heat loss predicted by the system codes varies from a low of 2.18 kW to a high of 5.91 kW.

Table 5. Operating and boundary conditions for benchmark Problem 3, Exercise 1C.

Parameters	Unit	Value
Heating power	KW	86.0
Helium mass flow rate	kg/s	0.1
Helium inlet temperature	K	380
Helium pressure	MPa	0.13
RCCS water mass flow rate	kg/s	0.33
RCCS water inlet temperature	K	313.15
RCCS water pressure	MPa	0.1
RCCS cavity air flow rate	kg/s	0.025
RCCS air inlet temperature	K	300

Table 6. Steady-state flow distribution (kg/s) calculated by five system codes.

Code	Inner Reflector	Inner Core	Middle Core	Outer Core	Outer Reflector
SAM	0.0039	0.0292	0.0332	0.0246	0.0090
RELAP5	0.0031	0.0260	0.0334	0.0286	0.0089
GAMMA+	0.0028	0.0230	0.0349	0.0304	0.0088
SPECTRA	0.0025	0.0207	0.0362	0.0305	0.0101
CNL-RELAP5	0.0034	0.0289	0.0343	0.0255	0.0079
CATHARE	0.0031	0.0283	0.0355	0.0251	0.0083

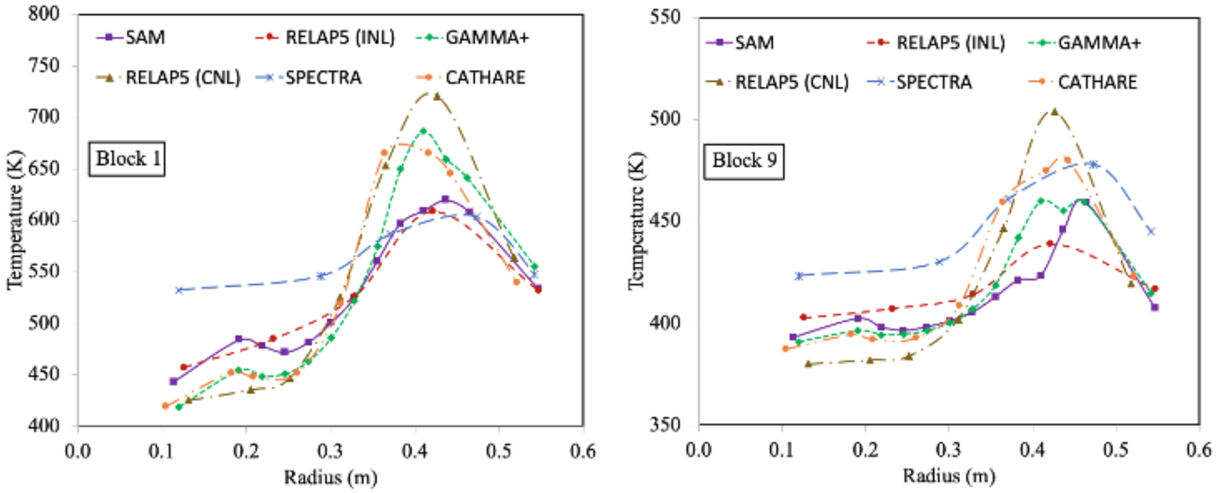

Figure 44. Helium temperature profiles in Blocks 1 and 9.

3.3.3. Pressurized Conduction Cooldown Results

After the circulator trips and forced flow is terminated, natural circulation is established in the core due to the temperature difference between the hotter outer region and colder inner region. Figure 45 shows the flow rates calculated by different system codes in different core regions during the PCC transient. Very good agreement (particularly between SAM and RELAP5) is observed among the codes, not only in the transient evolution but also in magnitude. Note that the flow rates immediately decline by more than three orders of magnitude from the steady-state flow rate (0.1 kg/s), and this is captured by all system codes. It is worth

Table 7. Steady-state heat removal in the RCCS (kW) calculated by five system codes.

Code	Water Panels	Air in Cavity	Total
SAM	4.09	1.17	5.26
RELAP5	2.63	0.49	3.12
GAMMA+	1.95	0.66	2.61
SPECTRA	4.70	1.21	5.91
CNL-RELAP5	1.48	0.70	2.18
CATHARE	2.62	0.92	3.54

mentioning that the very small natural circulation flow rate in the HTTF core is not necessarily representative of the PCC phenomenon in Modular High Temperature Gas-cooled Reactor (MHTGR) because helium pressure in the HTTF is one-tenth the nominal operating pressure in MHTGR. Because natural circulation flow is tiny in the HTTF, convective heat transfer is negligible. Consequently, the dominant modes of heat transfer in a PCC in the HTTF are thermal conduction and radiation.

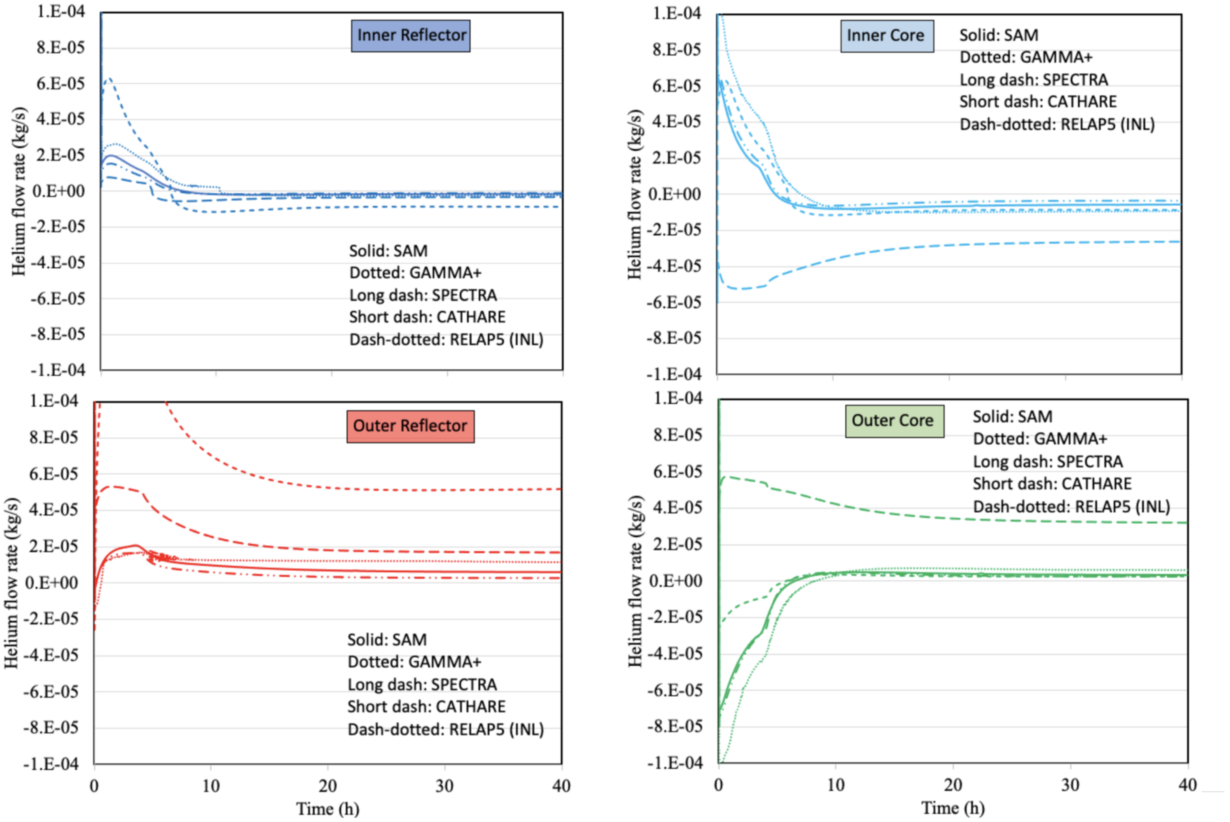

Figure 45. Natural circulation flow rates in different regions.

At the start of the transient, the heating power was first increased higher than the steady-state power for ~1.3 hours then gradually decreased to zero over the next 3 hours simulating decay heat in a reactor. After the heaters are completely turned off, the core cools down as heat is transferred to the reactor vessel and radiated to the RCCS. This transient behavior can be seen in Figure 46, which compares the temperatures in the ceramic Block 5 (core midplane) at four locations: inner reflector, inner core, middle core, and outer core. The following observations can be made:

- As expected, all models predict the correct transient temperature behavior in the middle and outer core, which is consistent with the heater rods heating history
- Although the inner reflector and inner core are not heated by heater rods, the temperature there also increases in the first part of the transient because of heat conduction from the heated outer core
- All models agree well in predicting the time to reach peak temperature in each location
- SAM (solid blue) and RELAP5 (dash-dot gray) results agree perfectly at all four locations throughout the 48 hour transient
- SPECTRA results are in good agreement with SAM and RELAP5 results in the inner, middle, and outer core locations
- GAMMA+, SAM, and RELAP5 agree well in the first few hours of the transient, reaching similar peak temperatures in unheated locations
- CATHARE peak temperatures are highest in all locations by ~150–200 K when compared to other models
- CNL-RELAP5 has the second highest peak temperatures, higher than SAM, RELAP5, GAMMA+, and SPECTRA by ~50–100 K.

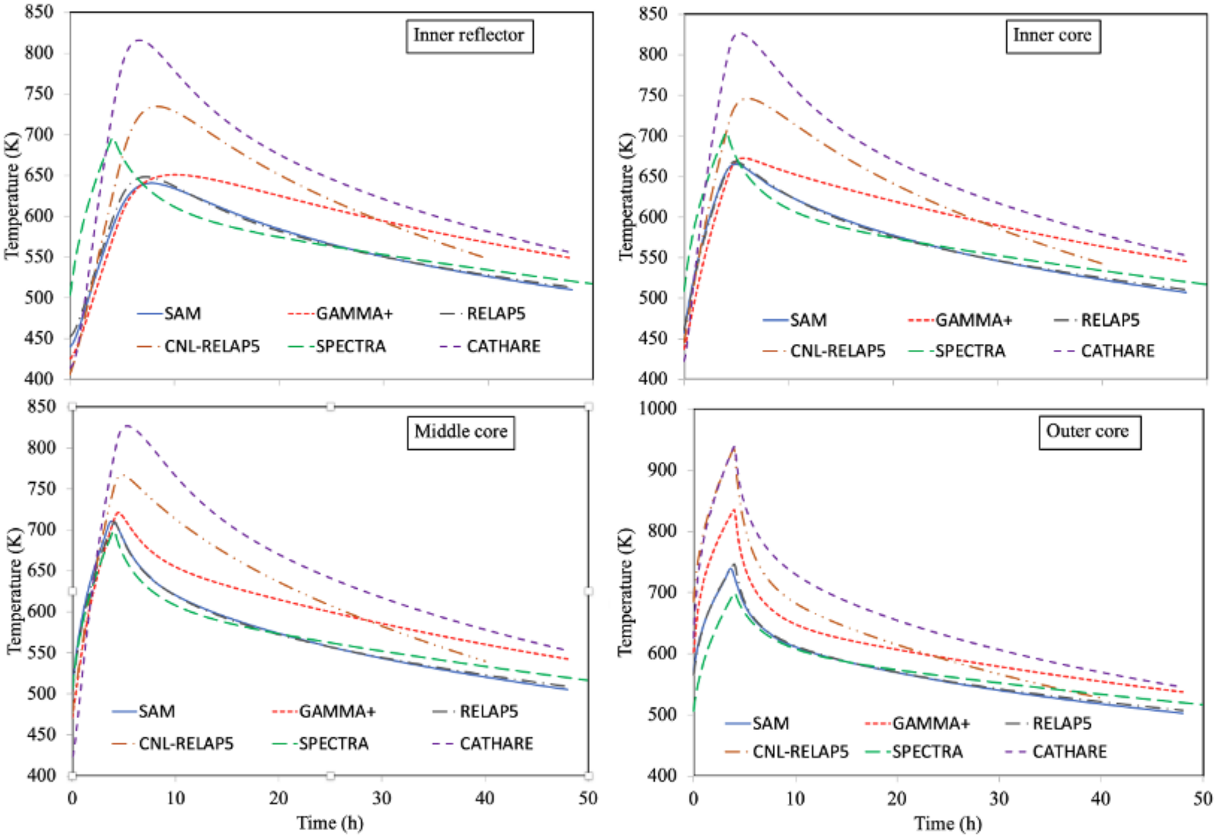

Figure 46. Transient temperature in the ceramic Block 5 (core midplane) at the inner reflector, inner core, middle core, and outer core.

The code-to-code comparisons of temperature in solids extend to the outer reflector, side reflector, core barrel, and reactor vessel shown in Figure 47. Besides similar features observed in Figure 46, other distinctive features observed in Figure 47 are:

- Due to heat loss from the reactor vessel, all models predict decreasing temperature in the outward radial direction
- The size of the differences in peak temperature in these outer locations is narrower than in the inner locations

- The CATHARE model predicts the highest peak temperature in the solids starting from the inner core through the core barrel and has the largest temperature gradient between the core barrel and reactor vessel
- In contrast to what was observed at the inner locations, CNL-RELAP5 peak temperatures at these outer locations are lower than most models
- The reactor vessel temperatures predicted by SAM, RELAP5, CATHARE, GAMMA+, and SPECTRA are close to each other (within 30 K). The CNL-RELAP5 temperatures are distinctly lower than the rest of the models.

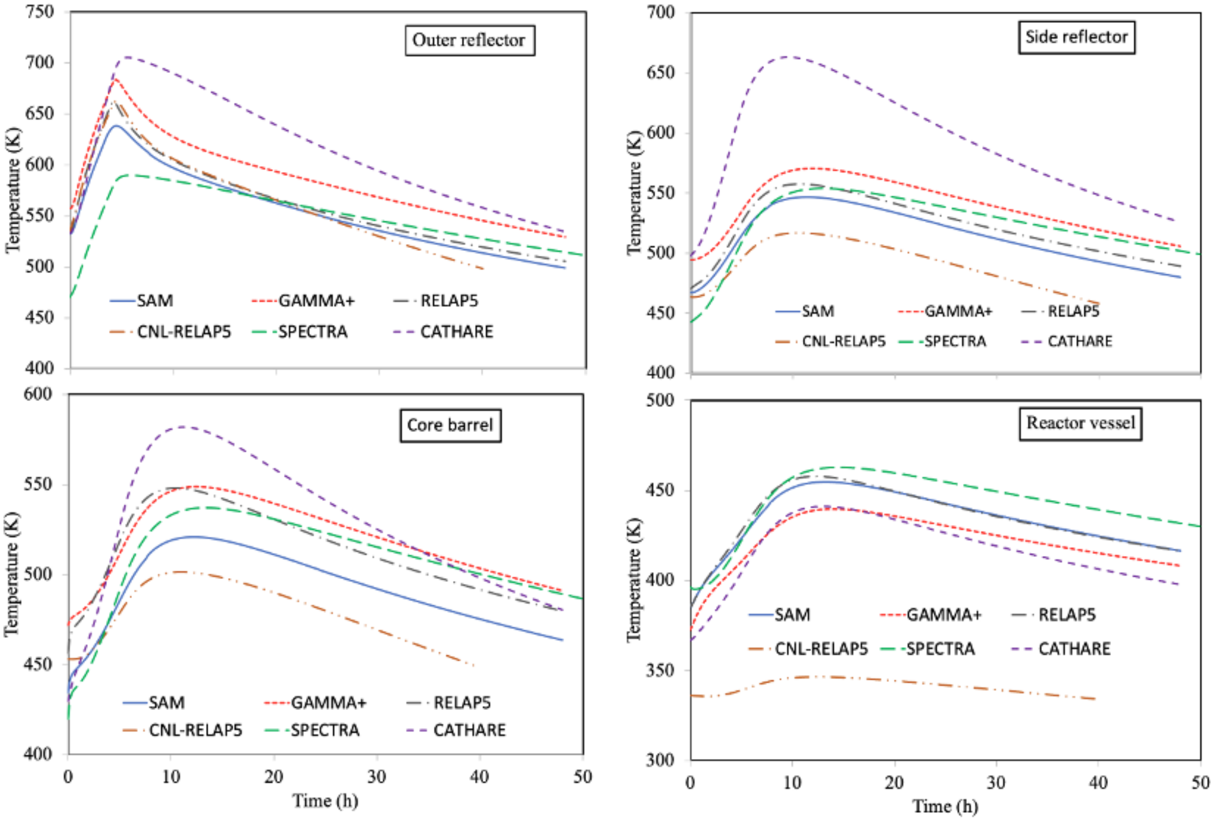

Figure 47. Transient temperature in the ceramic Block 5 (core midplane) at the outer reflector, side reflector, core barrel, and reactor vessel.

Figure 48 shows the transient heat removal in the RCCS by water panels and air flowing through the RCCS cavity. The transient behavior of heat removal in the water panels is very similar among SAM, RELAP5, SPECTRA, GAMMA+, and CATHARE and is consistent with the evolution of the reactor vessel temperature (i.e., increasing for ~13 hours before decreasing). The transient heat removal predicted by these models are offset by the value at steady state (t=0, also see Table 7). The CNL-RELAP5 model predicts a much lower reactor vessel temperature (Figure 47) and hence a correspondingly lower heat removal.

3.4. Problem 3---Exercise 2: Code-to-Data Comparison

In Exercise 2, participants simulate Test PG-27 under conditions that match the original experiments as closely as possible. Where necessary, they may use their judgment to define or adjust certain input variables and then validate results against Test PG-27 data. For instance, participants might specify the helium flow rate (not measured during the test) or adopt an effective core structural thermal conductivity different from

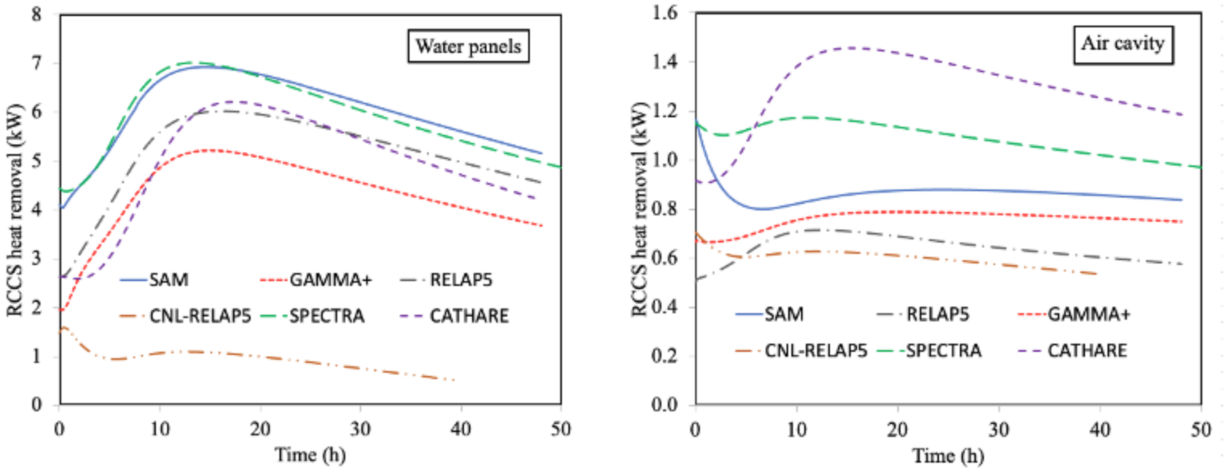

Figure 48. Heat removal by RCCS water panels and by air flowing through the cavity.

tabulated material property values to capture the complex thermal conduction behavior (due to the presence of hundreds of holes) of the HTTF in system-code modeling. Essentially, this exercise is similar to Exercises 1C and 1D but participants are given greater flexibility to calibrate the models when comparing with test data.

Temperature data for code validation were collected from thermocouples in three sectors: primary, secondary, and tertiary (Figure 39b). The secondary and tertiary thermocouples were positioned in locations equivalent to those in the primary sector to provide backup measurements. While consistent measurements across the three sectors would be ideal, the data revealed notable variations. These differences may be attributed to a variety of factors, such as misalignment or shifting of the core blocks, asymmetric experimental conditions, standard random and systematic uncertainties, data acquisition uncertainty, and uncertainties related to instrument alignment and location. Table 8 lists the identifiers of the thermocouples located on top of Blocks 3, 5, 7, and 9 in various core regions, the core barrel, and reactor vessel. Figures 49– 55 compare the simulation results submitted by the participants with Test PG-27 data.

Table 8. Thermocouple identification in the ceramic blocks, core barrel and reactor vessel.

Region	Sector	Block 3	Block 5	Block 7	Block 9
Inner reflector	Primary	TS-1302	TS-1502	TS-1702	TS-1902
	Secondary	TS-1316	TS-1516	TS-1716	TS-1730
	Tertiary	NA	NA	NA	NA
Inner core	Primary	TS-1303	TS-1503	TS-1703	TS-1903
	Secondary	TS-1317	TS-1517	TS-1717	TS-1917
	Tertiary	NA	NA	NA	NA
Middle core	Primary	TS-1305	TS-1505	TS-1705	TS-1905
	Secondary	TS-1319	TS-1519	TS-1719	TS-1919
	Tertiary	TS-1333	TS-1533	TS-1733	NA
Outer core	Primary	TS-1307	TS-1507	TS-1707	TS-1907
	Secondary	TS-1321	TS-1521	TS-1735	TS-1921
	Tertiary	NA	NA	NA	NA
Outer reflector	Primary	TS-1309	TS-1509	TS-1709	TS-1909
	Secondary	TS-1323	TS-1523	NA	TS-1923
	Tertiary	TS-1337	TS-1537	TS-1737	NA
Core barrel	—	TS-7102	TS-7103	TS-7104	NA
Vessel	—	TS-7402	TS-7403	TS-7404	NA

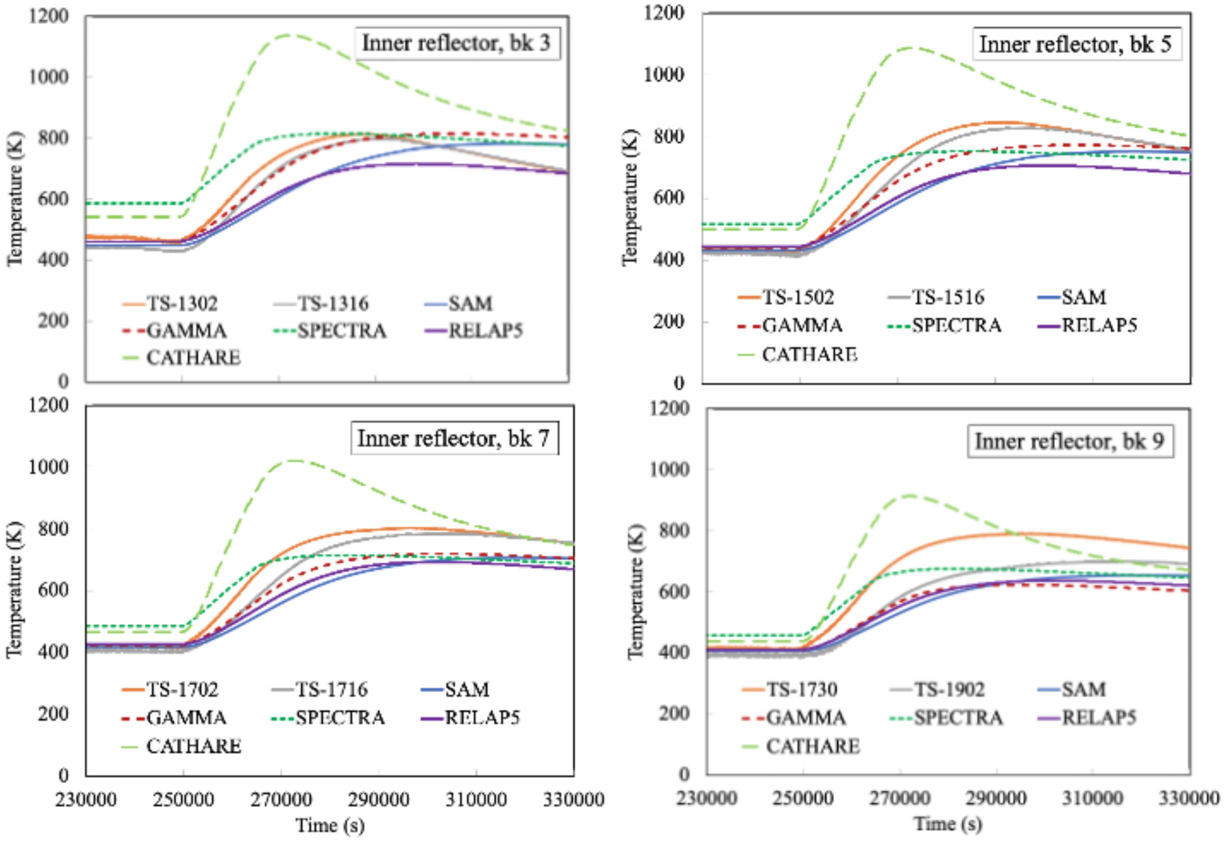

Figure 49. Code-to-data comparison of temperature at the inner reflector.

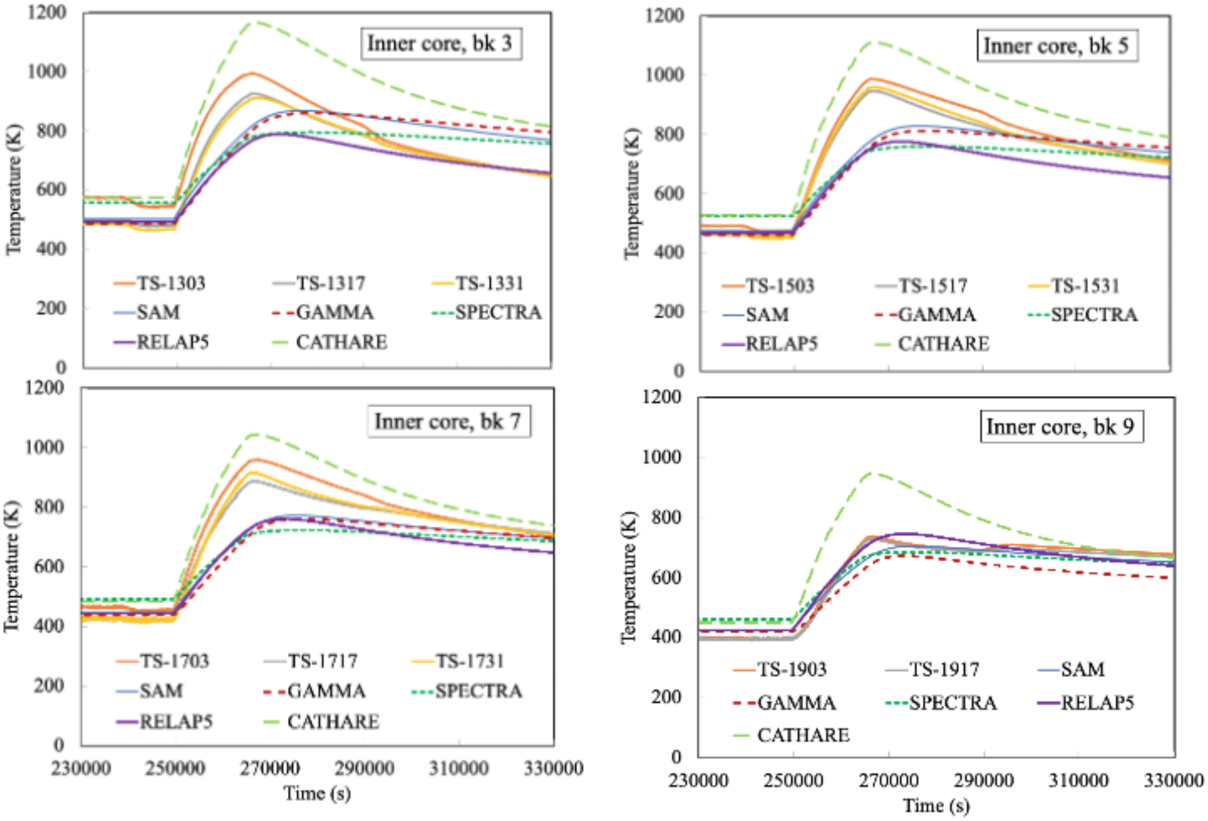

Figure 50. Code-to-data comparison of temperature at the inner core.

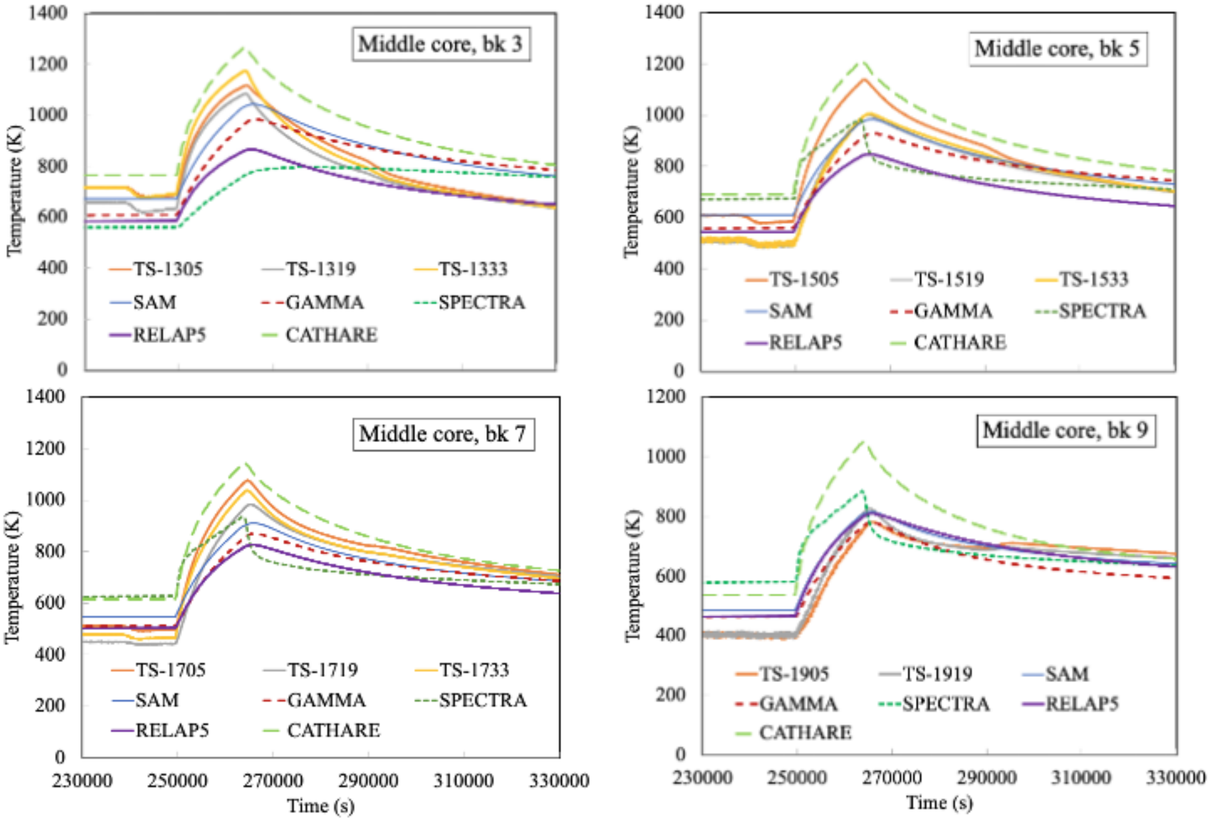

Figure 51. Code-to-data comparison of temperature at the middle core.

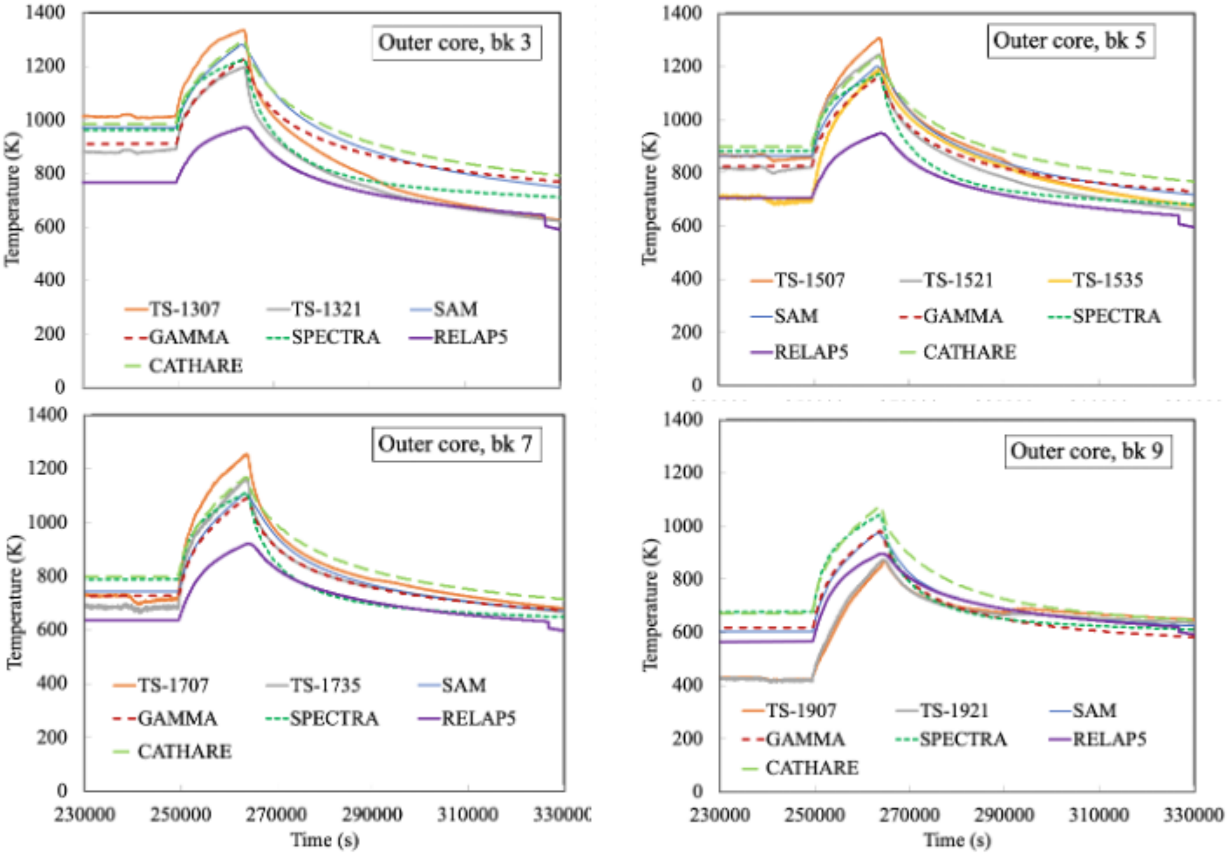

Figure 52. Code-to-data comparison at the outer core.

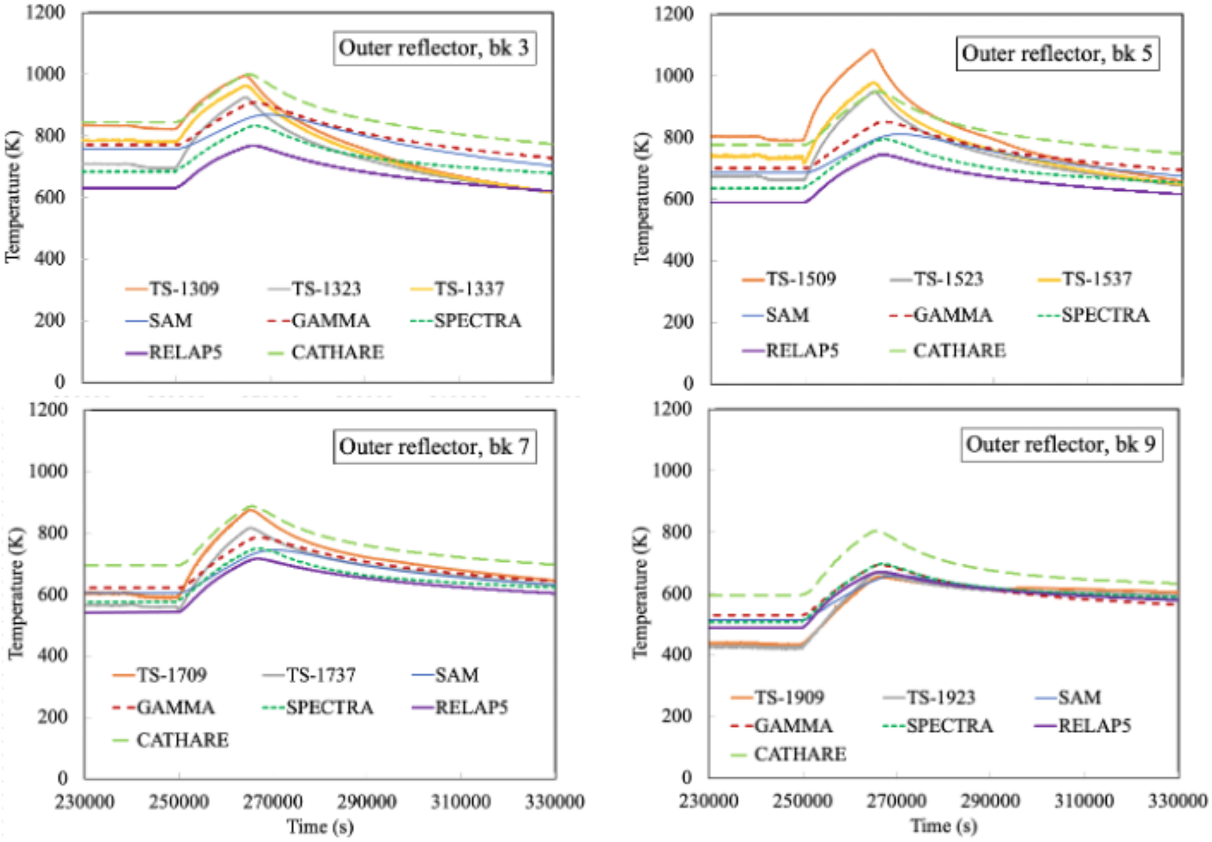

Figure 53. Code-to-data comparison of temperature at the outer reflector.

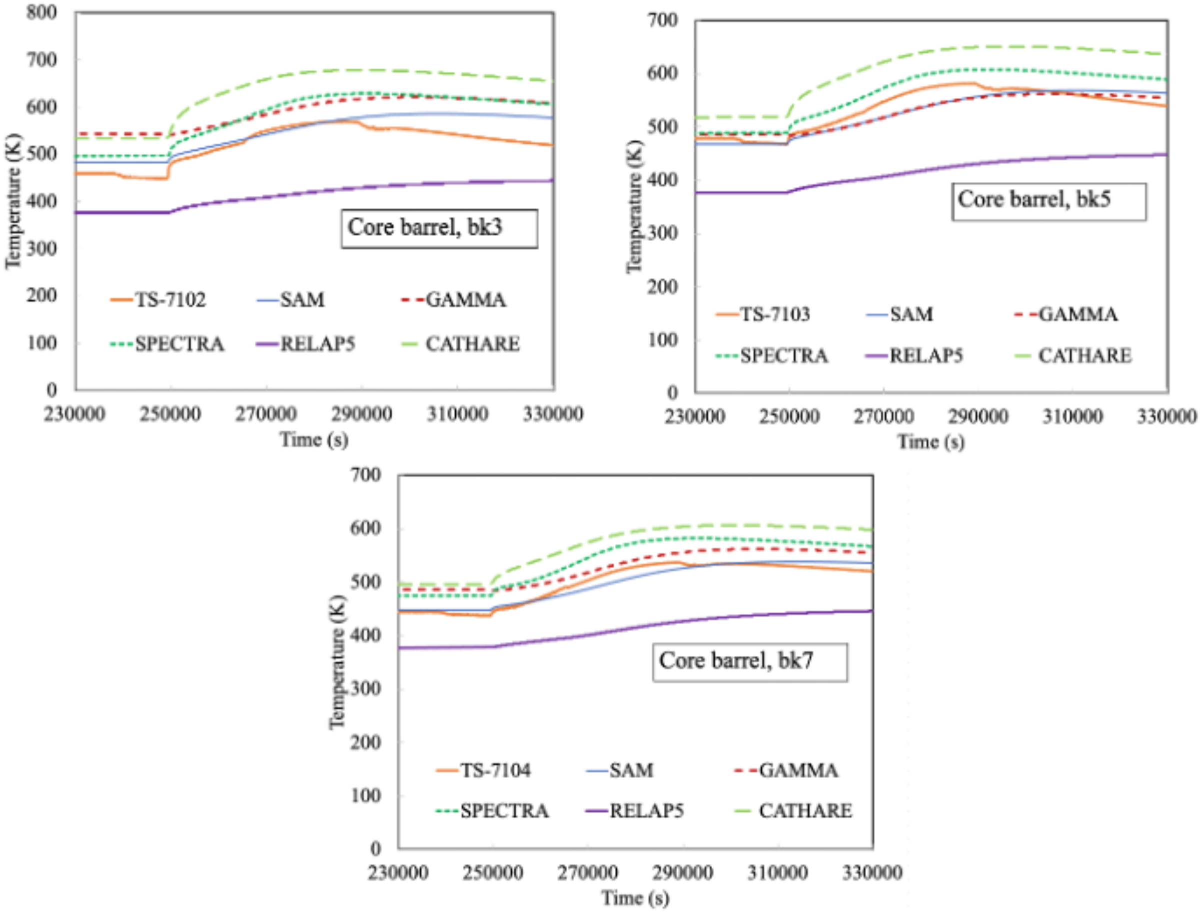

Figure 54. Code-to-data comparison of temperature at the core barrel.

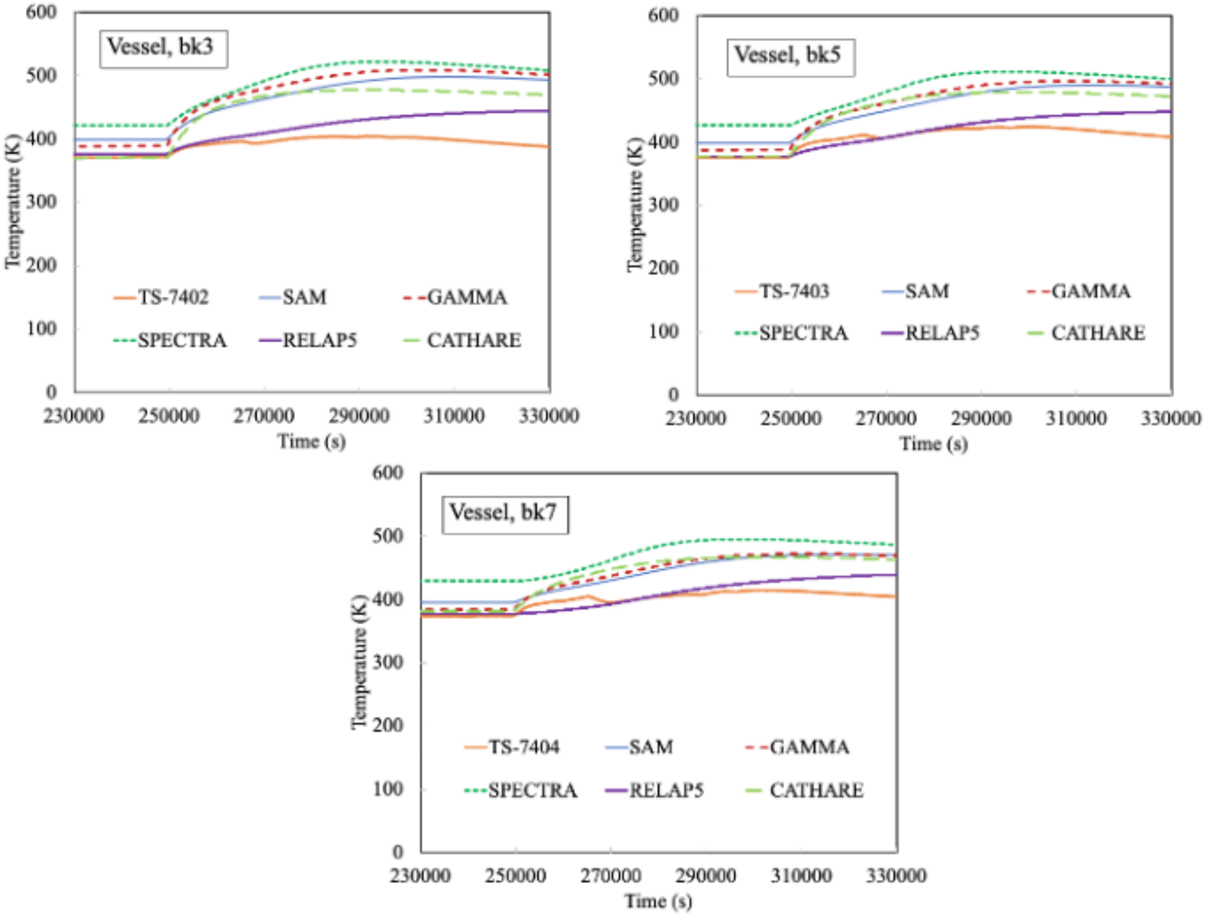

Figure 55. Code-to-data comparison of temperature at the reactor vessel.

4. CONCLUSIONS

This work presents the progress accomplished by the NEAMS HTGR application driver in FY25. The work presented in this report can be divided into three categories, namely 1) neutronics simulation of the GPBR200 with Griffin, 2) system-level simulation of the GPBR200 with SAM, and 3) thermal hydraulics simulation of the HTTF.

In the neutronics simulation of the GPBR200, in order to improve user experience, a new mesh generator was developed in Griffin to greatly simplify the specification of streamlines in the input file. Then, updates were presented with respect to the comparison of the running-in simulations between Griffin and *kugelpy*. Of particular interest was a scenario with sharp interfaces between regions in the pebble bed where the pebble composition changes. Generally, a good agreement was obtained between the *kugelpy* and Griffin results where parameters such as the maximum power density and *k*-eff from both sets of simulations matched each other relatively well. Despite that, a closer inspection revealed that the relative difference between the predicted fission rates from both models showed relatively large differences. Furthermore, the online cross-section generation capability that was recently introduced to Griffin was evaluated against *kugelpy* for a running-in simulation. Even though the general agreement between the two sets of simulation was good, some differences were observed, such as the persistent bias in the *k*-eff predicted by the Griffin model before 80 days and the underprediction of the spike in the maximum power density when the equilibrium fuel was introduced. Next, preliminary studies were performed to investigate the effects of including control rods at the top of the core using *kugelpy*.

In the second part of the report, the GPBR200 was modeled using the SAM core channel approach where the pebble-bed region was modeled using individual core channels. An attempt was made to model the cross flow in the pebble bed due to in-core natural circulation during the PLOFC transient. However, due to the numerical instability issue, the cross flow model was not implemented in SAM. Nevertheless, an engineering approach was used to capture the effects of cross flow. Using the results from the SAM 2D porous media model as a reference, the updated core channel model showed an improved prediction of the pebble temperature during the PLOFC transient. Furthermore, the wall channeling effect due to higher porosity in the near wall region was investigated. The study showed that the higher porosity near the wall had an effect on the flow distribution in the core during the PLOFC. With variable porosity near the wall, the pebble temperature during the PLOFC was noticeably higher due to lower helium flow in the hot inner region of the core. Next, a steady-state coupled multiphysics simulation was performed using the SAM core channel model and a Griffin model with the online cross-generation capability. The preliminary study showed that the coupled model worked well. Nevertheless, several possible improvements were identified and would be implemented in a future work.

In the third part of the report, a thermal hydraulics analysis of the HTTF was presented, which was a part of the OECD/NEA thermal-hydraulic code validation benchmark activity for an HTGR. A CFD simulation was performed using NekRS to investigate the flow mixing problem in the lower plenum of the HTTF. The study revealed the complex phenomena in the lower plenum, such as pronounced local acceleration, recirculation, and interactions with constraining structures, resulting in sustained velocity and temperature fluctuations downstream. Furthermore, as a part of the OECD/NEA benchmark activity, code-to-code and code-to-data comparisons were performed for Test PG27, which is a PCC test, between five codes, namely SAM, RELAP5, GAMMA+, SPECTRA, and CATHARE, across six organizations from five countries. Generally, the different simulations showed good agreement in terms of the general trend but differences were observed in terms of some parameters such as the peak temperatures of different regions and heat removal rate.

For future work, the following will be considered:

- **Griffin running-in modeling**: This report documented the first investigation into online cross-section generation for a running-in simulation with Griffin. The online cross-section capability had been used previously for an equilibrium core, but a number of updates were required for it to work for a running-in simulation. After the updates, the capability is now available; however, some accuracy issues have been noted that will be addressed in future work. As the online cross-section capability becomes more mature for running-in simulations, the benchmark models with control rods developed for this work will be useful in the future for further code-to-code verification studies.

- **SAM core channel model**: The core channel model will continue to be developed, particularly on the enhancement of the cross flow model. In addition to the pressurized and de-pressurized loss of forced cooling transients, other scenarios such as air ingress into the core will also be demonstrated. Furthermore, for the demonstration of the online cross-section generation capability in Griffin, a new coupling approach will be implemented to improve the exchange of information between the nodes in the SAM model and the elements in the Griffin model. Additionally, the coupled model will also be extended to transient scenarios.
- **CFD HTTF model**: Future work will integrate our standalone nekRS simulations into the HTTF benchmark framework by conducting systematic code-to-code comparisons with other CFD solvers, followed by code-to-data validation against HTTF experimental measurements. Key activities will include rigorous uncertainty quantification through mesh and timestep refinement studies, an assessment of alternative turbulence models, and an exploration of conjugate heat transfer coupling to capture solid–fluid interactions. Ultimately, this work will demonstrate how high-fidelity CFD can inform reactor design tasks for HTGRs.
- **System-level HTTF model**: The OECD/NEA benchmark activity will be concluded along with the completion of the final report.

Page intentionally left blank

5. REFERENCES

[1] E. Mulder and W. Boyes, “Neutronics characteristics of a 165 MWth Xe-100 reactor,” *Nuclear Engineering and Design*, vol. 357, p. 110415, 2020.

[2] N. Stauff, C. Lee, and C. Filippone, “Core design of the holos-quad microreactor,” tech. rep., Argonne National Laboratory (ANL), Argonne, IL (United States), 2022.

[3] W. R. Stewart, E. Velez-Lopez, R. Wiser, and K. Shirvan, “Economic solution for low carbon process heat: A horizontal, compact high temperature gas reactor,” *Applied Energy*, vol. 304, p. 117650, 2021.

[4] S. Schunert, J. Ortensi, Y. Wang, P. Balestra, M. Jaradat, O. Calvin, J. Hanophy, and L. Harbour, “An equilibrium core depletion algorithm for pebble-bed reactors in the griffin code,” *Annals of Nuclear Energy*, vol. 192, p. 109980, 2023.

[5] J. Hanophy, P. Balestra, Y. Wang, J. Ortensi, and S. Schunert, “Multiphysics Running-In Simulations for Pebble-Bed Reactors with Griffin,” *Nuclear Science and Engineering*, vol. 0, no. 0, pp. 1–15, 2025.

[6] G. L. Giudicelli, A. Abou-Jaoude, A. J. Novak, A. Abdelhameed, P. Balestra, L. Charlot, J. Fang, B. Feng, T. Folk, R. Freile, T. Freyman, D. Gaston, L. Harbour, T. Hua, W. Jiang, N. Martin, Y. Miao, J. Miller, I. Naupa, D. O’Grady, D. Reger, E. Shemon, N. Stauff, M. Tano, S. Terlizzi, S. Walker, and C. Permann, “The Virtual Test Bed (VTB) Repository: A Library of Reference Reactor Models Using NEAMS Tools,” *Nuclear Science and Engineering*, vol. 0, no. 0, pp. 1–17, 2023.

[7] Z. M. Prince, P. Balestra, J. Ortensi, S. Schunert, O. Calvin, J. T. Hanophy, K. Mo, and G. Strydom, “Sensitivity analysis, surrogate modeling, and optimization of pebble-bed reactors considering normal and accident conditions,” *Nuclear Engineering and Design*, vol. 428, p. 113466, 2024.

[8] D. Reger, E. Merzari, P. Balestra, R. Stewart, and G. Strydom, “Discrete element simulation of pebble bed reactors on graphics processing units,” *Annals of Nuclear Energy*, vol. 190, p. 109896, 2023.

[9] J. Zhang, F. Li, and Y. Sun, “Physical Analysis of the Initial Core and Running-In Phase for Pebble-Bed Reactor HTR-PM,” *Science and Technology of Nuclear Installations*, vol. 2017, 2017.

[10] R. Stewart, J. Cavaluzzi, P. Balestra, and G. Strydom, “Capturing the run-in of a pebble-bed reactor by using thermal feedback and high-fidelity neutronics simulations,” *Annals of Nuclear Energy*, vol. 207, p. 110697, 2024.

[11] J. T. Hanophy, R. H. Stewart, P. Balestra, Z. J. Ooi, J. Fang, T. Hua, and L. Zou, “High-temperature gas-cooled pebble-bed reactors running in and transient modeling capabilities demonstration,” Tech. Rep. INL/RPT-25-82868, Idaho National Laboratory and Argonne National Laboratory, September 2024.

[12] R. Stewart, P. Balestra, D. Reger, E. Merzari, and G. Strydom, “High-fidelity simulations of the run-in process for a pebble-bed reactor,” *Annals of Nuclear Energy*, vol. 195, p. 110193, 2024.

[13] H. Park, Y. S. Jung, C. Lee, Y. Wang, and J. Ortensi, “Initial assessment of online cross section generation capability of Griffin for gas-cooled pebble-bed reactor,” in *Proceedings of the international conference on physics of reactors-PHYSOR 2024*, (San Francisco, CA), pp. 642–653, 4 2024.

[14] W. van Antwerpen, R. G. Rousseau, and C. G. du Toit, “Multi-sphere Unit Cell model to calculate the effective thermal conductivity in packed pebble beds of mono-sized spheres,” *Nuclear Engineering and Design*, vol. 247, pp. 183–201, 2012.

[15] E. Merzari, H. Yuan, M. Min, D. Shaver, R. Rahaman, P. Shriwise, P. Romano, A. Talamo, Y. Lan, D. Gaston, *et al.*, "Cardinal: A lower-length-scale multiphysics simulator for pebble-bed reactors," *Nuclear Technology*, vol. 207, no. 7, pp. 1118–1141, 2021.

[16] A. Novak, R. Carlsen, S. Schunert, P. Balestra, R. Slaybaugh, and R. Martineau, "Pronghorn: A multidimensional coarse mesh application for advanced reactor thermal-hydraulics," *Nucl. Tech.*, vol. 207, pp. 1015–1046, 2021.

[17] S. Schunert, P. Balestra, R. Carlsen, M. DeHart, R. Martineau, and A. Novak, "Coupling of Pronghorn and RELAP-7 for a Pebble Bed Reactor," Tech. Rep. INL/CON-19-54415-Rev000, Idaho National Laboratory, August 2020.

[18] R. Stewart, D. Reger, and P. Balestra, "Demonstrate Capability of NEAMS Tools to Generate Reactor Kinetics Parameters for Pebble-Bed HTGRs Transient Modeling," Tech. Rep. INL/EXT-21-64176, Idaho National Laboratory, August 2021.

[19] Z. Ooi, L. Zou, T. Hua, J. Fang, and R. Hu, "Modeling of a Generic Pebble Bed High-temperature Gas-cooled Reactor (PB-HTGR) with SAM," Tech. Rep. ANL/NSE-22/59, Argonne National Laboratory, 2022.

[20] Z. Ooi, L. Zou, T. Hua, J. Fang, and R. Hu, "Multi-Physics System-level Simulations of a Generic Pebble Bed High-Temperature Gas Cooled Reactor with Coupled SAM/Griffin Model," Tech. Rep. ANL/NSE-23/45, Argonne National Laboratory, 2023.

[21] J. T. Hanophy, R. H. Stewart, J. Fang, T. Hua, L. Zou, and P. Balestra, "High-temperature gas-cooled pebble-bed reactors running in and transient modeling capabilities demonstration," tech. rep., Idaho National Laboratory (INL), Idaho Falls, ID (United States), 2024.

[22] L. Zou and R. Hu, "Recent SAM Code Improvement to Heat Transfer Modeling Capabilities," Tech. Rep. ANL/NSE-19/46, Argonne National Laboratory, 2019.

[23] W. van Antwerpen, C. G. Du Toit, and P. G. Rousseau, "A review of correlations to model the packing structure and effective thermal conductivity in packed beds of mono-sized spherical particles," *Nuclear Engineering and Design*, vol. 240, no. 7, pp. 1803–1818, 2010.

[24] T. D. Roberto, C. M. Lapa, and A. C. Alvim, "Scaling analysis of reactor cavity cooling system in htr," *Nuclear Technology*, vol. 206, no. 4, pp. 527–543, 2020.

[25] D. R. Gaston, C. J. Permann, J. W. Peterson, A. E. Slaughter, D. Andrš, Y. Wang, M. P. Short, D. M. Perez, M. R. Tonks, J. Ortensi, L. Zou, and R. C. Martineau, "Physics-based multiscale coupling for full core nuclear reactor simulation," *Annals of Nuclear Energy*, vol. 84, pp. 45–54, 2015.

[26] D. Reger, E. Merzari, P. Balestra, S. Schunert, Y. Hassan, and H. Yuan, "An improved pressure drop correlation for modeling localized effects in a pebble bed reactor," *Nuclear Engineering and Design*, vol. 403, p. 112123, 2023.

[27] R. Hu, L. Zou, T. Mui, D. O'Grady, E. Cervi, Z. J. Ooi, G. Yang, T. Fei, G. Hu, G. Zhang, *et al.*, "SAM Theory Manual," tech. rep., Argonne National Laboratory (ANL), 2025.

[28] I. W. Gutowska and Brian, "OSU High Temperature Test Facility Design Technical Report," Tech. Rep. OSU-HTTF-TECH-003-R2, Oregon State University, Corvallis, Oregon, May 2019.

[29] A. S. Epiney *et al.*, "Overview of HTTF Modeling and Benchmark Efforts for Code Validation for Gas-Cooled Reactor Applications," in *Fourth International Conference on Generation IV Small Reactors (G4SR-4)*, (Toronto, ON, Canada), October 2022.

[30] R. Kile *et al.*, "Code Benchmark in Depressurized Conduction Cooldown Transient in the High Temperature Test Facility," in *Advances in Thermal Hydraulics (ATH) Conference*, (Orlando, FL), November 2024.

[31] S. Cadell and B. Woods, "OSU High Temperature Test Facility Test Acceptance Test Report: PG-27 Lower Power (<350 kW) Complete Loss of Flow, 2 Heaters," Tech. Rep. OSU-HTTF-TAR027-R, Oregon State University, 2019.

[32] T. Hua, R. Kile, S. N. Lee, L. Zou, and A. Epiney, "Code Benchmark of Pressurized Conduction Cooldown Transient in the High Temperature Test Facility," in *2024 International Congress on Advances in Nuclear Power Plants (ICAPP)*, June 2014.

[33] S. J. Ball and F. E. Fisher, "Next Generation Nuclear Plant Phenomena Identification and Ranking Tables (PIRTs) Volume 1: Main Report," Tech. Rep. NUREG/CR-6944, U.S. NRC, 2008.

[34] J. Fang, D. R. Shaver, A. Tomboulides, M. Min, P. Fischer, Y.-H. Lan, R. Rahaman, P. Romano, S. Benhamadouche, Y. A. Hassan, *et al.*, "Feasibility of full-core pin resolved cfd simulations of small modular reactor with momentum sources," *Nuclear Engineering and Design*, vol. 378, p. 111143, 2021.

[35] D. Shaver, A. Obabko, A. Tomboulides, J. Fang, H. Yuan, Y. Yu, S. Tutwiler, D. Dai, N. Saini, and C. Boyd, "Nek5000: improvements in the available RANS models, meshing, tutorials, and training," Tech. Rep. ANL/NSE-21/79, Argonne National Laboratory, Lemont, IL, 2021.

[36] H. Yuan, Y. Yu, and D. Shaver, "Development of A Quadratic Tet-To-Hex Conversion for Pure Hexahedral Mesh: Application to Nuclear Engineering," in *19th International Topical Meeting on Nuclear Reactor Thermal Hydraulics (NURETH-19)*, 2022.

Nuclear Science and Engineering Division
Argonne National Laboratory
9700 South Cass Avenue
Lemont, IL 60439

www.anl.gov